1	Seismo-acoustic Characterization of the 2018 Sierra Negra Caldera Resurgence and
2	Fissure Eruption in the Galápagos Islands
3	
4	Hugo D. Ortiz ^{1,2,3} , Robin S. Matoza ¹ , Benjamin Bernard ⁴ , Rodrigo De Negri ^{1,5} , and Mario
5	C. Ruiz ⁴ .
6	¹ Department of Earth Science and Earth Research Institute, University of California, Santa
7	Barbara, Santa Barbara, CA, USA, ² Facultad de Ciencias Exactas y Naturales, Pontificia
8	Universidad Católica del Ecuador, Quito, Ecuador, ³ Department of Earth, Atmospheric and
9	Planetary Sciences, Massachusetts Institute of Technology, Cambridge, MA, USA, ⁴ Instituto
10	Geofísico, Escuela Politécnica Nacional, Quito, Ecuador, ⁵ Laboratoire Magmas et Volcans,
11	Université Clermont Auvergne, Clermont-Ferrand, France
12	Corresponding author: Hugo D. Ortiz (<u>hdortiz@mit.edu</u>)
13	
14	Key Points:
15 16	• We identify possible premonitory signals ~2 hours before the main eruptive phase of Sierra Negra.
17	• We quantify the migration of the eruption down the north flank of the volcano.
18 19 20	 We document new sources of infrasound in an area where access is challenging, and eruptive fissures have not been mapped.

Abstract

The 2018 eruption of Sierra Negra volcano, Galápagos, Ecuador has provided new insights into the mechanisms of caldera resurgence, subsidence, and fissuring at basaltic shield volcanoes. Here, we integrate local (~0.4 km) seismo-acoustic records and regional (~85 km) infrasound array data to present new observations of the 2018 Sierra Negra eruption with improved time and spatial resolutions. These observations include: air-to-ground coupling ~2 hours before the time of the eruption onset, migration of the infrasound tremor from 22:54 June 26 to 12:31 June 27 UT (all times in UT), and persistent infrasound detections during the weeks between 5 July and 18 August from an area that does not coincide with the previously documented eruptive fissures. We interpret air-to-ground coupling as infrasound tremor generated in the nearby fissures before the main eruptive phase started, although ambiguity remains in interpreting a single seismic-infrasonic sensor pair. The progressive location change of the infrasound tremor agrees with the migration of the eruption down the north flank of Sierra Negra at a rate of $\sim 0.15 \pm 0.04$ m/s. The weeks-long persistent detections coincide with a region that has thermal anomalies, co-eruptive deformation, lava fields, and geological features that could be interpreted as multiple lava tube skylights. Our observations and interpretations provide constraints on the mechanisms underlying fissure formation and magma emplacement at Sierra Negra.

Plain Language Summary

During volcanic eruptions, the expulsion of molten rock and gases produces vibrations of the ground and the atmosphere. These vibrations are known as seismic and infrasound waves, which we record in specialized sensors. Using these records, along with deformation data and satellite imagery, we study the 2018 eruption of Sierra Negra in the Galápagos Islands in detail. We utilize seismic and infrasound records to a) identify premonitory signals ~2 hours before the main eruptive phase of Sierra Negra, b) quantify the migration of the eruption down the north flank of the volcano, and c) document new sources of infrasound in an area where access is challenging, and eruptive fissures have not been mapped. Our observations contribute to an improved understanding of the mechanisms during fissure opening, eruption, and migration. Such mechanisms are perhaps unique to the volcanoes in the Galápagos since fissure development is not limited by shallow rift zones as occurs at many other basaltic systems (e.g., Kīlauea, Piton de la Fournaise, Cumbre Vieja). We highlight the advantage of integrating seismic, infrasound, deformation, and satellite observations for improved geophysical volcano monitoring at shield volcanoes.

1. Introduction

68 69 70

71

72 73

74 75

76 77

78

79

80

81

82 83

84

85

86

87

88

89

Advances in infrasound infrastructure and methods have allowed the characterization of the volcanic acoustic wavefield from local (<15 km) to regional (15-250 km) to remote (>250 km) ranges (e.g., Johnson and Ripepe, 2011; Fee and Matoza, 2013; Matoza et al., 2018; Johnson, 2019; Marchetti et al., 2019; Watson et al., 2022; Matoza and Roman, 2022). Most studies of regional and remote range volcanic infrasound observations have naturally focused on explosive eruptions, as these are more energetic and capable of producing infrasound that can be detected above noise at these distances (e.g., Fee et al., 2010; Matoza et al. 2011; Matoza et al., 2022; Perttu et al., 2023, McKee et al., 2021). Effusive eruptions are less commonly detected at ranges >15 km since their lower-amplitude signals are less likely to be recorded in the tropospheric diffraction zone and beyond (e.g. Garcés et al., 2003; Fee and Garcés, 2007; Matoza et al., 2009, 2010; Ripepe et al., 2018; Barrière et al., 2023). The majority of infrasound studies of effusive eruptions recorded locally (<15 km) have focused on Kīlauea, Hawaii and associated vents. Kīlauea infrasound studies have demonstrated the capabilities of infrasound arrays to detect continuous infrasound tremor originating at Pu'u'Ō'ō and lava tubes (Garcés et al., 2003; Matoza et al., 2010). More recently infrasound from Kīlauea has been used to track fissure migration (Fee et al., 2011; Thelen et al., 2022), monitor caldera collapses (Thelen et al., 2022), differentiate activity originating at the vent from high-speed lava flows interacting with the atmosphere (Lyons et al., 2021), and estimate lava fountain jet velocity and diameter (Gestrich et al., 2022). The seismo-acoustic study by Lai et al., (2021) provided evidence of the shallow seismic sources during the 2018 Kīlauea activity, including constraints on magma migration, source location, and length of the conduit above the Halema'uma'u reservoir.

90 91

92

93

94 95

96 97

98

99

100101

102

103

104

105

106

107

108

109

110

Sierra Negra, an 1140 m high basaltic shield volcano, in the Galápagos, Ecuador has been much less studied and characterized than Kīlauea or Piton de la Fournaise in the literature to date (e.g., Patrick et al., 2019; Hilbert et al., 2015; Peltier et al., 2022), and this provides new opportunities to improve knowledge of the seismo-acoustics of basaltic shield volcanoes and their eruption mechanisms. Moreover, considering that at volcanoes in the Galápagos, lava extrusion occurs at radial and circumferential fissures widely scattered around the calderas without showing a dominant location or direction (Chadwick and Howard, 1991), it becomes necessary to develop methods and test geophysical networks for determining the location of active fissures during ongoing eruptions. This is especially true when compared to other shield volcanoes (e.g., Mauna Loa, Kīlauea, Cumbre Vieja, Piton de la Fournaise), where magma migration and emplacement are predominantly controlled by shallow rift zones (Dieterich, 1988; Tilling and Dvorak, 1993; Carracedo, 1994; Anguita and Hernán, 2000), which generally limit the area for the opening of new eruptive fissures and vents. As a result, forecasting where and when new eruptive fissures will open has proven to be challenging, and near (< 1 km) seismo-acoustic observations have remained elusive in the Galápagos and elsewhere. Hence, our very near-to-source (~0.4 km) and regional (~85 km) seismo-acoustic observations of fissure activity in 2018 provide insights into the geophysical processes ocurring during the phase preceding the eruption, the lava fountain, and the migration of the eruption down the flank of Sierra Negra volcano. Additionally, our study helps understand the evolution of fissures, identify their geophysical signatures, and interpret degassing mechanisms that might have taken place during their opening.

Sierra Negra has the largest caldera (9.5x7.5 km wide and 100 m deep) among the volcanoes in the Galápagos islands (Figure 1). Eruptions at Sierra Negra in 2005 and 2018 were preceded by years of inflation, indicating the progressive magma recharge of a flat-topped sill-like reservoir located ~2 km below the caldera floor (Jónsson et al., 2005; Yun et al., 2006; Bell et al., 2021b). In 2005 and 2018, earthquakes of moment magnitude (Mw) 5.5 and 5.4, respectively, occurred hours before the eruptions (Geist et al., 2008; Bell et al., 2021a). These earthquakes resulted from the rupture and slip of the intra-caldera fault system (Geist et al., 2008; Bell et al., 2021a), which acts as a trapdoor fault (Amelung et al., 2000). During the 2005 eruption, most of the lava flows were constrained inside the caldera, as all five vents feeding the eruption were also located inside the caldera; only a small area on the north flank was covered by lava that resulted from spatter of two energetic vents (Geist et al., 2008). In 2018, the focus of this study, the eruption was preceded by 5.2 m of caldera uplift and the subsequent eruptive subsidence was in some regions of up to 8.5 m (Bell et al., 2021a; Davis et al., 2021). Currently, eruption reports (Vasconez et al., 2018; Davis et al., 2021; Bell et al., 2021a) indicate that the five closest fissures to the caldera rim were active for less than 24 hours, and after a short quiescence, the farthest fissure was active for a little less than two months. Lava flows erupted from a fissure system extended over the north flank, covering an area of 30.6 km² (Vasconez et al., 2018); the highest fissure intersects the caldera rim, while the lowest vent is about 90 m above sea level (Davis et al., 2021).

Figure 1. Geological and geophysical observations of the 2018 eruption of Sierra Negra volcano in the Galápagos Islands. a) Map of Sierra Negra, showing the eruptive fissures (orange lines and numbers), the intra-caldera fault system (blue dashed lines), individual earthquakes (black dots after Bell et al., 2021a), and the approximate location of the pre-eruptive seismic tremor (region bounded by the green dashed line after Li et al., 2022). We highlight the two large magnitude 5 earthquakes (red circles) as well as earthquakes of magnitude 4 (purple circles) occurring two hours before the reported eruption onset (Stage II). Local geophysical observations comprise two GPS stations (blue squares) and one seismo-acoustic station (blue triangle). b) We complement the local (~0.4 km) seismo-acoustic observations from VCH1 with data from the regional (~85 km) infrasound array IS20 (blue triangles). c) Caldera of Sierra Negra as seen from the east (location indicated with letter P in panel a).

Deformation, seismicity, petrology, and satellite observations of the 2018 Sierra Negra eruption have revealed a 1.5 m resurgence of the caldera floor (Bell et al., 2021a), the eruption was fed by a 15 km long sill (Davis et al., 2021), the pre-eruptive seismic tremor is not related to sub-surface magma flow but rather generated by a slowly propagating fracture (Li et al., 2022), seismic velocity changes prior to the eruption (Ruiz et al., 2022), and that the stress evolution of the rock surrounding Sierra Negra's magma system can help forecast the eruption onset (Gregg et al., 2022). Further, Shreve and Delgado (2023) investigated and assessed the conditions leading to the caldera subsidence of Sierra Negra in 2018; they suggest that slip along the trapdoor fault system is the initial stage before a full scale caldera collapse. Also, using deformation and seismic data, Bell et al. (2021b) showed how the volcano edifice reacts to the increasing magma volume stored in the shallow sill. While these observations have substantially improved our knowledge of Sierra Negra, we still have much to learn of the flank magma intrusion processes, including fissure formation and magma emplacement to surface. This is particularly important because the recent studies have been unable to detect seismicity related to the opening and eruption of the fissure system (Bell et al., 2021a), maybe because as suggested by Li et al. (2022) the pre-eruptive seismic

tremor (Figure 1a) stops when the eruption begins and magma flows silently to the surface without further rock fracturing. In addition, from our knowledge of the two previous eruptions at Sierra Negra, the location and the orientation of the fissures in 2018 were unexpected. The 1979 and 2005 eruptions took place at fissures close to the volcano summit and oriented parallel to the caldera rim (Geist et al., 2008), while fissures in 2018 did not show a preferential orientation with locations spanning from the caldera rim to up to 9.5 km away (Davis et al., 2021). Nonetheless, we show that our seismo-acoustic observations can aid in better understanding the 2018 fissure eruption, with the potential to track infrasound from active fissures that, in most of the cases, are reported only when a visual confirmation was possible (Bernard et al., 2022) or later during field mapping campains (Bell et al., 2021a).

Here we integrate local (~0.4 km) seismic-acoustic observations of the 2018 Sierra Negra effusive eruption with regional (~85 km) infrasound observations. We also discuss how the additional uncertainties due to the propagation and back azimuth determination play a role while quantifying the eruption chronology.

2. Data & Methods

We analyze data from VCH1, a seismic-acoustic station in the permanent network of the Instituto Geofísico, Escuela Politécnica Nacional (Alvarado et al., 2018); the station has a three-component Trillium Compact 120 seismometer and a MB2005 microbaramoter, recording the seismic and acoustic wavefields at 100 Hz and 50 Hz, respectively. VCH1 is located ~0.4 km from the where the eruption begun, and the seismic and acoustic sensor are less than 5 metters apart. In addition, we use infrasound data from station IS20, which is part of the International Monitoring System (IMS) infrasound network. The IS20 station is on the Santa Cruz Island (Galápagos) about 85 km from Sierra Negra (Figure 1b). The station has eight MB3a microbarometers with minimum and maximum element spacing of 0.36 and 2.00 km, respectively. IS20 is sampled at 20 Hz and began operating in December 2017.

In the discussion section we compare our seismo-acoustic results with GPS and satellite data. GPS data show pre-ruptive and co-eruptive deformation at stations GV03 and GV06 located inside the Sierra Negra caldera (Bell et al., 2021a; Geist et al., 2002; Figure 1a). Satellite data are comprised of Interferometric Satellite Amplitude Radar (InSAR) imagery (Davis et al., 2021; Figure 6) and near infrared observations (Ortiz et al., 2024; Figure 7). From the InSAR data we outline the areas of deformation and their change as the eruption migrated down the flank of Sierra Negra, whereas we utilize near-infrared satellite observations to constraint the activity at Fissure 4 and track hotspots in its close proximity.

2.1 Back azimuth determination and uncertainty

Given the array distribution of the microbarometers at IS20, we apply the Progressive Multi-Channel Correlation (PMCC) method (Cansi, 1995) to detect and obtain the direction of arrival of coherent signals. Specifically, we use 15 log-spaced frequency bands and time-windows (Figure S1), following Matoza et al. (2013).

PMCC detections show a rich multi-frequency infrasound wavefield (Figure 2). The eight microbarometers at IS20 combined into fifty-six unique triads (subnetworks) independently help to determine the direction of arrival of coherent signals to the array. Between 26 June and 19 August 2018, we find more than 29100 PMCC infrasound detections arriving from the direction of Sierra Negra (250°-270°). During the first few hours of the eruption we detect infrasound signals from the region where Fissure 1 (257.0°) intersects the caldera rim. These dections then migrate down the flank of the volcano toward Fissure 4 (261.5°).

Figure 2. Infrasound detections at IS20 of the 2018 eruption of Sierra Negra; we draw the average back azimuth to Fissures 1 and 4 (horizontal dotted lines) with respect to IS20.

Uncertainty quantification on back azimuth and trace velocity estimates are key to understanding the limitations of infrasound arrays to recover spatial information of the source location. Uncertanties have an elliptical geometry, which depend on the spatial distribution of the acoustic sensors and the sampling rate. The minimum and maximum uncertainties correspond to the minor and major axes of the error ellipse, with uncertainty varying as a function of back azimuth. For IMS arrays, the Cramer-Rao Bound (CRB) is the standard method used to compute the uncertainties on back azimuth and trace velocity estimates (CEA, 2016). For instance, at IS20, assuming infrasound crossing the array at 340 m/s, the uncertainties of back azimuths are between 0.20° and 0.26°. Further, evaluating the uncertainties with the method proposed by Szuberla and Olson (2004), we obtain uncertainties between 0.75° and 1.10°, when also 340 m/s is assumed for sound speed. Although, both methods lead to relatively small uncertainties, in section 4.4, we show that back azimuth uncertainties at IS20 are close to CRB estimates; we use satellite imagery of hotspots and earthquake epicenters to verify the location of several acoustic sources recorded during the eruption of Sierra Negra in 2018.

2.2 Theory and applications of seismo-acoustic coupling

During eruptions, in addition to incident seismic and acoustic waves from the volcano, waves propagating through the Earth-atmosphere interface are recorded at receivers (e.g., Palacios et al., 2016; Ichihara 2016; Nishida and Ichihara, 2016; Muramatsu et al., 2022). To distinguish air-to-ground transmission, we compute seismo-acoustic cross-correlation (Ichihara et al., 2012), and coherence and phase spectrograms (Matoza and Fee, 2014). Coherence and phase spectrograms are the counterparts in the frequency domain of cross-correlation, with the advantage that they provide a detailed view of coupling in the whole frequency range. These methods are based on the theory developed by Ben-Menahem and Singh (1981) of acoustic waves in the atmosphere refracting into the Earth; acoustic waves induce vertical ground motion, which is recorded, at two perfectly co-located seismic and acoustic sensors, a quarter of cycle (90°) after the pressure wave (see also Anthony et al., 2022).

Ichihara et al., (2012) demonstrated that the cross-correlation function (R) between waveforms of the vertical seismic velocity (W) and acoustic pressure (P) is approximately equal to:

$$R[\tau; W, P] \sim R[\tau; w_{in}, p_{in}] + R[\tau; w_{in}, H_{wp}w_{in}] + R[\tau; H_{pw}p_{in}, p_{in}]$$
 (1)

where w_{in} and p_{in} are the incident seismic and acoustic wavefields, H_{wp} is the transfer function for ground-to-air coupling, H_{pw} is the transfer function for air-to-ground coupling, and τ is the delay of W respect to P. Ichihara et al., (2012) assumes that wind noise is uncorrelated for seismic and acoustic sensors with a small separation. In Equation (1), the first cross-correlation term becomes significant only when incident seismic and acoustic waves share a common source, and it reaches the maximum value for $\tau < 0$. The second term is the correlation between the vertical seismic velocity and the corresponding ground-to-air coupled signal $(H_{wp}w_{in})$; it has a maximum correlation for $\tau = 0$ (i.e., 0° phase shift), since H_{wp} is a real number. The third term is the cross-correlation between the transmitted air-to-ground signal and the acoustic pressure, and it reaches a maximum for $\tau = 1/(4f_0)$ (i.e., 90° phase shift); where f_0 is the characteristic frequency of the incident pressure wave.

Using the theory developed for air-to-ground coupling, new applications have been proposed to better help quantify volcanic eruptions. Ichihara (2016) computed the transfer function (H_{pw}) to correct seismic records from air-to-ground coupled waves and evaluate scaling laws that related seismic power and magma discharge. In parallel, Nishida and Ichihara (2016) similarly computed H_{pw} to derive infrasound waveforms from seismic records and compare to independent results inferred from infrasound array processing. Further, Ichihara et al., (2021) presented a method to systematically compute the air-to-ground transfer function and used the results to correct Volcanic Seismic-Acoustic Ratios (VASR; Johnson and Aster, 2005), which generally are used to investigate the energy partitioning between seismic and acoustic wavefields. Other developments (McKee et al., 2018; Bishop et al., 2023) have shown that a pair of seismic and acoustic sensors, where seismo-acoustic coupling is recorded, can be used to estimate the direction of arrival of infrasound waves.

In Section 3.2, we apply seismo-acoustic cross-correlation, coherence, and phase spectrum analysis to study the onset of the 2018 Sierra Negra eruption.

3. Results

3.1 Eruption report and definition of eruptive stages of Sierra Negra.

On 16 January 2018, the Secretaria Nacional de Gestión de Riesgos y Emergencias (Ecuador) declared a yellow alert due to the increased seismicity and deformation found at Sierra Negra (Bernard et al. 2022). The next day, the rangers at the Galápagos National Park closed the access to the southeast section of the caldera rim. As the eruption of Sierra Negra appeared to be imminet, multiple ashmeters and seismometers were installed at the volcano as well as a gravity survey was carried out in early 2018 (Bell et al., 2021a; Bernard et al., 2022). In the morning of 26 June 2018 at 9:15 a large Mw5.4 earthquake was localized inside the caldera of Sierra Negra (Figure 1a), and on the same day, a special report from Instituto Geofisico was issued, indicating that the large earthquake and seismic tremor could be precursors to an eruption. Following an intense earthquake swarm generally located inside the caldera of Sierra Negra (Figure 1a), the eruption was confirmed at 19:45 by a large thermal anomaly observed in satellite data and visual observations of lava fountains made by the park rangers (Bernard et al., 2022).

Generally, the eruption has been divided into two phases according to fissure activity (Vasconez et al., 2018; Bell et al., 2021a; Davis et al., 2021). The first phase corresponds to lava effusion through Fissures 1, 2, 3, 5, and 6 (Figure 1a), only lasting less than 24 hours between 26 and 27 June 2018. While in the second phase lava extrusion took place at Fissure 4 (Figure 1a) between 1 July and 25 August 2018.

However, to describe the distinct eruptive episodes and in turn explain our seismo-acoustic observations, we divide the eruption chronology into five stages. Below we provide the times and dates, including brief descriptions of each phase to orient the reader throughout this document. Detailed phase descriptions and corresponding discussions are provided in the subsequent subsections.

- Stage I (09:15-17:40 June 26): consists of only seismicity dominated by individual earthquakes.
- Stage II (17:40-19:40 June 26): air-to-ground coupling is detected at VCH1.
- Stage III (19:40 June 26 16:45 June 28): the eruption starts and air-to-ground coupling continues at VCH1. This stage exhibits high-amplitude acoustic and seismic tremors, with acoustic emissions from Sierra Negra detected at both VCH1 and IS20.
- Stage IV (16:45 June 28 00:29 July 05): the volcano undergoes a period of near-quiescence with only a few acoustic detections at IS20.
- Stage V (00:30 July 05 00:00 August 19): the volcano begins a long-lived lava extrusion at Fissure 4 with persistent infrasound detections in its vicinity.

3.2 Seismo-acoustic analysis at VCH1 during the 2018 Sierra Negra eruption.

We perform seismo-acoustic analysis on data recorded on 26 June 2018 at VCH1. Here, in the main document we only present the analysis corresponding to the beginning of the eruption, from 13:00 to 23:59 on 26 June 2018 (all times in UTC; Figure 3). In the supplemental information (Figure S2) we conduct the same seismo-acoustic analysis to data from the first half of June 26 to show the background activity preceding the seismic swarms, tremors, and eruption. To compute seismo-acoustic cross-correlations (Figure 3b), we use 10-s sliding windows with 50% overlap; waveforms are prefiltered in the 1-24 Hz frequency band using a 4-pole Butterworth filter. Similarly, using 10-s sliding windows with 50% overlap, we compute coherence and phase spectrums as well as seismic and acoustic spectrograms on unfiltered waveforms (Figures 3c-f). We remove the instrumental response of seismic and acoustic sensors beforehand and we make a time correction to account for the separation between the seismic and acoustic sensors assuming plane wave propagation.

Figure 3. Seismo-acoustic analysis of data recorded at VCH1 from 13:00 to 23:59 on 26 June 2018. a) Seismic and infrasound waveforms filtered between 1 and 24 Hz. For plotting, we clip the high amplitude impulsive acoustic and seismic waveforms to better show the background activity. Inset shows individual earthquakes (spikes) embedded in the cigar shaped wind noise (purple lines). The same cigar shape is observed on the infrasound records. b) Cross-correlogram between the seismic and infrasound signals shown above. c) Seismo-acoustic coherence and d) phase spectrograms. e) Seismic and f) infrasound spectrograms. Panels from c to f use raw

unfiltered waveforms. At ~19:40 (vertical black, blue, and white lines), Vasconez et al. (2018), Bell et al. (2021a), and Bernard et al. (2022) report the beginning of the eruption of Sierra Negra.

339

340

341342

343

344

345

346

347

348

349

350

351

352

353

354

355

356

357

358

359

360

361

362

363

364

365

366

367368

369

370371

372

373374

375

376377

378379

380

381

382

383

On 26 June 2018, high-rate seismicity starts hours before the eruption (Stage I), then transitions into seismic tremor interspersed with large amplitude earthquakes (Stage II), and finally, the eruption begings at ~19:40 (Stage III) (Bell et al., 2021a; Li et al., 2022; Figures 3 and S2). In Stage I, at 09:15, an earthquake of moment magnitude 5.4 ruptures the southern flank of the trapdoor fault, triggering individual quakes distributed mostly along this c-shaped fault (Figures 1a and S2; Bell et al., 2021a). Seismicity that is relatively small in amplitude between approximately 13:00 and 16:30 (Figure 3e), coincides with subtle coupling at frequencies of ~14-17 Hz and phase ~0° (green band in Figure 3d); individual earthquakes are embedded in the cigar shaped wind noise recorded in the seismic sensor (inset, Figure 3a). At the end of Stage I, from 17:00 to 17:40, seismicity increases in rate and amplitude with seismo-acoustic coupling continuing at frequencies of ~14-17 Hz and phase ~0°; this seismic swarm is located in the northwest corner of the trapdoor (Bell et al., 2021a; Figure 1a). At 17:40, at the begining of Stage II, discrete earthquakes initially in the northwest corner of the intra-caldera fault system migrate eastward toward the first eruptive fissure and southward along the western trapdoor fault (Bell et al., 2021a). During Stage II, acording to Bell et al. (2021a), there are five magnitude 4 earthquakes distributed along the intra caldera fault system and, as shown by Li et al. (2022), there is also a pre-eruptive seismic tremor locate ~10 km from VCH1 (Figure 1a). Toward 19:35, seismic tremor glides to higher frequencies (Figure 3e). The frequency gliding can also be seen in the coherence, phase, and infrasound spectrograms (Figures 3c,d,f). Over these ~2 hours (Stage II), coherence and in turn cross-correlation reach a maximum, while the corresponding phase spectrogram indicates multi-band frequency coupling. The most significant bands are ~1-14 Hz with phase shift of $\sim 90^{\circ}$ (orange band in Figure 3d) and $\gtrsim 15$ Hz with phase of $\sim 0^{\circ}$ (green band in Figure 3d). Around 19:40 (beginning of Stage III), the seismic tremor energy focuses on a narrower frequency band until 20:00, when again tremor becomes broadband. Since ~19:40, coupling continues with a dominant phase delay of ~90° and starting at 20:00 an additional narrow frequency band at ~5 Hz indicates coupling with phase of $\sim 0^{\circ}$ (Figure 3d).

From 17:40 to 19:40 (Stage II), in the infrasound spectrogram, we observe predominant spectral bands at frequencies of ~10-15 Hz and later starting at 20:00 (Stage III), the acoustic energy mostly focuses at ~2-3 Hz (Figure 3f). This change in frequency is also visible in the seismo-acoustic correlogram (Figure 3b), which according to Ichihara et al. (2012) depends on the characteristic frequency (f_o) of the air-to-ground coupled signal, with maximum cross-correlations at $\tau = 1/(4f_o)$. For the high-frequency tremor the maximum correlations are at $\tau = \sim 0.07 \, s$, while for the low-frequency tremor are at $\tau = \sim 0.4 \, s$. This frequency change manifests as narrower banding of maximum correlations in Stage II, which transitions to broader banding at times later than 20:00, during Stage III (Figure 3b).

We extend the analysis from a few hours at the beginning of the eruption to several days. In addition to spectrograms and coherence, we include Root Mean Square (RMS) amplitudes of seismic and infrasound data recorded at VCH1 between 26 June and 6 July 2023 (Figures 4a-c). The spectrograms are computed using 5 min windows with 95% overlap, while RMS amplitudes and coherence are computed for 10 min windows with 25% overlap. Coherence and spectrograms

are derived from unfiltered waveforms, whereas RMS amplitudes are obtained from filtered waveforms within the frequency band of 1-8 Hz.

The infrasound RMS amplitudes and spectrogram do not show a clear trend of the evolution of the Sierra Negra eruption in 2018, while their seismic counterparts can track the main phases of the eruption (Figures 4a-c). For instance, spikes in the seismic RMS and spectrogram are the major earthquakes that occur before and during the eruption, while sustained increase in amplitude, on June 26-27 (Stages II and III) and near the end of July 1 (Stage IV), relate to the pre-eruptive and eruptive tremors (Figures 4a and 4b). These eruptive features are not clear in the infrasonic RMS and spectrogram (Figures 4a and 4c), possibly because wind noise levels are high at VCH1 and the low-amplitude nature of the effusive volcanism of Sierra Negra in 2018. Moreover, coherence captures very well the high similarity of the seismic and acoustic waveforms during the two hours preceeding the eruption (Stage II) and then from the eruption onset until approximately 12:31 June 27 (first half of Stage III). The high coherence indicates seismo-acoustic coupling in Stages II and III, which is likely dominated by air-to-ground coupling, as shown in Figure 3d.

In the next subsection, we supplement our local observations at VCH1 with infrasound data from IS20. We identify coherent detections and corresponding back azimuths and trace velocities that relate to eruption in Sierra Negra during stages I, III, IV, and V (Figures 4d-f).

3.3 Analysis of the 2018 Sierra Negra eruption using the IS20 infrasound array.

We use numerical timestamps to highlight features in the infrasound dectections at IS20 and distinguish the projections of relevant back azimuths on the map (Figures 4d-f). These features include the dection of the large magnitude five earthquakes occurring at the beginning of Stages I and V, the back azimuth migration down the flank of the volcano during Stage III, sparse acoustic detections during Stage IV, and long-lasting detections during Stage V. There are not acoustic detections at IS20 during Stage II. We place eight numerical labels in the following chronological order (Figure 4d): (1) The 5.4 Mw earthquake preceding the eruption is recoded at 9:19 on June 26, with back azimuth within 0.2° of the seismic inferred location. (2) At 19:45, on the same day, we first identify a persistent infrasound tremor arriving from the summit of Sierra Negra. The back azimuth corresponding to the tremor, remains constant and equal to 257.0°; (3-4) then progressively shifts from 257.0° to 260.7° between 22:54 June 26 and 12:31 June 27. (5) For the next 28 hours the eruption continues along the fissure system until it stops at 16:45 on June 28. (6) After a few days of acoustic quiescence, we detect sporadic infrasound signals between 2 and 4 July, with back azimuths between 260° and 264°, which point to fissures mapped on the field. (7) At 00:34 on July 5, we register a 5.1 Mw earthquake prior to (8) persistent infrasound detections from back azimuth 263°. This back azimuth generally agrees with the location of Fissure 4, which is at about 11 km northwest of the eruption onset (Figure 4f); acoustic emissions from this region continue until August 18 with some periods of acoustic quiescence. Time stamps provided in this paragraph are respect to IS20. To find times at the origin (Sierra Negra), an approximate 4 min travel time correction needs to be applied, but slightly varies depending on the infrasound source location.

Figure 4. Integration of local seismo-acoustic observations from VCH1 and regional infrasound data from IS20 for tracking the eruption onset and eruption migration along the north flank. a)

Average coherence and seismic and acoustic root mean square amplitudes computed using 10-minute windows with 25% overlap of data recorded in VCH1. b) Seismic and c) infrasound spectrograms of VCH1 data. d) Back azimuth and c) trace velocity as function of time and frequency derived at IS20. The red arrows and numbers (1-8) correspond to chronological events described in the main text. f) Projected back azimuth for the Mw 5.4 earthquake (252.8°; blue arrow), migration of the eruption down the north flank (257.0°-260.7°; black arrows), and location of the long-lasting eruptive fissure (263°; green arrow). Red lines indicate the lava flows from the different fissures (Vasconez et al., 2018) and the blue dot indicates the epicenter of the main earthquake (Bell et al., 2021a). Vertical blue and white lines indicate the eruption onset (~19:40 June 26, 2018).

3.4 Comparison of local and regional seismo-acoustic observations

Most of the acoustic activity is recorded at both VCH1 and IS20 stations; however, there are instances where the data from one of the sites provides additional detail on the eruption chronology. In Stages I and V, the two large magnitude five earthquakes are recorded at both stations, but only at IS20 we infer the direction to their source. During Stage II, the acoustic waves recorded as air-to-ground coupling at VCH1 are not detected at IS20, possibly because the generation mechanism is weak and the attenuation over the ~85 km travel path is strong. The onset of the eruption (Stage III) is recorded at both stations, but there is a latency of about 4 minutes at IS20 due to the infrasound travel time from the Isabela to Santa Cruz Islands. Furthermore, when the acoustic sources propagate down the flank of the volcano these location variations are detected as back azimuth and trace velocity changes at IS20.

4. Discussion

4.1 Interpretations of seismo-acoustic coupling at VCH1 during the eruption onset of Sierra Negra

Following the theory proposed by Ben-Menahem and Singh (1981) and extended by Ichihara et al. (2012), we differentiate three types of seismo-acoustic coupling during the beginning of the 2018 Sierra Negra eruption, from Stage I to Stage III (Figure 3). We detect high-frequency ground-to-air coupling, broadband frequency air-to-ground coupling, and low-frequency ground-to-air coupling as follows: Starting in the second half of Stage I and continuing until the end of Stage II (13:00-19:35), we identify ground-to-air coupling at high-frequencies (~14-17 Hz; green bands in Figure 3d). Then, from the beginning of Stage II (17:40) and continuing through Stage III, we observe a 90° phase shift of the seismic signal with respect to infrasound (orange bands in Figure 3d) and high seismo-acoustic coherence as shown in the correlogram and coherence spectrograms (Figures 3b and 3c); this is consistent with air-to-ground transmission. Finally, close to the beginning of Stage III (20:00), we detect ground-to-air coupling at low frequencies (~5 Hz) with the characteristic phase shift of ~0° between seismic and acoustic waveforms, while coherence is almost imperceptible (Figure 3c). This low-frequency ground-to-air coupling continues throughout 26 June 2018.

Next, we provide brief explanations of the low- and high-frequency ground-to-air coupling. While we dedicate additional space to interpreting the air-to-ground coupling in Stage II because this

signal has the characteristics of infrasound tremor and might provide information on fissure formation and eruption precursors of Sierra Negra.

4.1.1 Interpretations of the low- and high-frequency ground-to-air coupling during Stages I, II, and III

We regard the high-frequency ground-to-air coupling observed in Stages I and II (13:00-19:35), as mechanical vibrations of the microbarometer (e.g., Alcoverro et al., 2005; CEA-Martec, 2007; Nief et al., 2019) induced by earthquakes and seismic tremor occurring in close proximity to VCH1. This follows, after considering the laboratory experiments performed by Merchant and McDowell (2014) that indicate MB2005 pressure sensors are sensitive to mechanical shaking at frequencies above 7 Hz.

More interestingly, in Stage III, we observe low-frequency ground-to-air coupling at \sim 5 Hz (Figure 3d). Since the MB2005 microbarometers are not sensitive to ground motion in the low frequency range, we relate the coupling to seismic energy refraction at the solid Earth-atmosphere boundary and recorded on the pressure sensor. In accordance with the theory developed by Ichihara et al., (2012), we observe a phase delay of \sim 0° and coherence coefficients smaller than the ones associate with air-to-ground coupling.

4.1.2 Interpretation of air-to-ground coupling during Stage II

Considering the 90° phase delay of seismic waves with respect to infrasound is indicative of airto-ground coupled waves at VCH1. We can interpret these coupled waves as subtle infrasound tremor generated at the nearby fissure system that is only recorded locally. This ensues from taking account recent observations of the different phases during fissure eruptions in Hawai'i (Houghton et al., 2021) and Iceland (Hjartardóttir et al., 2023), where degassing progressively increased before the more energetic magmatic phase. Houghton et al., (2021) describes this phase as continuous but pulsating outgassing that on occasions can resemble gas jetting, whereas Hjartardóttir et al., (2023) show snapshots of steam outflux that gradually escalate at five vents before their magmatic phase. Pulsating degassing, gas jetting, and vigorous steam plumes can produce infrasound and might explain the acoustic wavefield we detect at VCH1 before 19:40. For instance, fumarole studies at Aso (McKee et al., 2017) and Iwo-Yama (Yamakawa et al. 2023) volcanoes show that these gas rich volcanic emissions can produce coherent and observable infrasound usually at high frequencies (> 7 Hz). Our infrasound records at Sierra Negra also show continuous infrasound at frequencies ≥ 10 Hz between 17:40 and 19:40 (Figure 3f), with frequencies of ~10-15 Hz that dominate the seismo-acoustic correlogram (Figure 3b). Concurrently, from 17:40 to 19:40, there is frequency gliding observed in both seismic and infrasound tremors (Figures 3e-f). As shown by Spina et al., (2022) in laboratory experiments and observed at volcanoes (e.g., Sciotto et al., 2022), frequency gliding can occur before eruptions transition to a more explosive and energetic phase. Furthermore, at 17:40 also the caldera floor of Sierra Negra starts undergoing a massive deformation that in some regions is up to 1.5 m (Figure 5a). This large deformation might have signaled the opening of the trapdoor allowing magma to exit from the sill to the shallow plumbing system. Possibly existent magma pathways created during the 2005 eruption were quickly re-occupied and activated during the 2018 eruption since

one of the fissures is common to both eruptions. All these observations suggest that air-to-ground coupled waves observed before 19:40 at VCH1 might correspond to infrasound tremor generated by strong degassing, just before the magmatic phase. To our knowledge these could be the first seismo-acoustic observations, reported in the literature, of the opening of a fissure eruption, including transitions from subtle degassing to gas jetting to the magmatic phase.

526527528

521522

523524

525

The interpretation of Stage II is challenging and some ambiguity remains due to the complexity of the seismic and acoustic signals (Figures 5b-c). Thus, next, we offer additional interpretations for some of the observed seismic and infrasound features.

529530531

532

533

534

535

536

537

538

539

540

541

542

543

544

545

546

547

548

549

550

551

552

553

554

555

556

557

558

559

560

The spectral bands and gliding that appear in the seismic and infrasound records (Figures 3d-f) might not be related to harmonic emission tremor. It is possible that highly similar small repetitive events recorded at regular intervals are mimicking harmonic tremor through the well-known "Dirac comb" effect (e.g., Gordeev, 1993; Hagerty et al., 2000; Powell and Neuberg, 2003). Further, the acceleration of the rate of these similar quakes can make the spectral lines glide upwards (e.g., Powell and Neuberg, 2003; Hotovec et al., 2013) or conversely the deacceleration of the rate of events can make the spectral lines glide downwards as observed in Figure 3e. However, an in-depth analysis of the discrete events recorded between 17:40 and 19:40 is needed to study their similarity and interevent times to further explore this hypothesis. Another explanation for the seismic spectral lines and gliding, although not documented in the literature, is that time-varying site and path responses are modifying the seismic records at VCH1. Perhaps the meter-scale deformation that Sierra Negra undergoes over a few hours (Figure 5a) is drastically affecting the ground, producing the observed time-dependent spectral peaks (Figures 3e). As the properties of the medium change, it is conceivable that different frequency-dependent attenuations and resonances dominate over time. In a similar basaltic system, Hotovec-Ellis et al. (2022) interpret seismic velocity changes as being related to the opening, closing, or creation of cracks; they suggest that rapid ground deformation related to the pressurization of the magma reservoir can strongly affect the fracture fabric in the surrounding rocks. Thus, it is possible that site and path effects might have varied during the deformation observed at Sierra Negra, influencing the seismic waveform shape. In addition, we observe mechanically induced infrasound transients which are simultaneously recorded with earthquakes (Figures 5b-c). These induced transients highly modify our infrasound record, making difficult an unambiguous interpretation of the acoustic wavefield with a single infrasound sensor. Since the MB2005 microbarometers are sensitive to ground motions for frequencies higher than 7 Hz (Merchant and McDowell, 2014), it is possible that some of the features we observe in the infrasound spectrogram are affected by the shaking of the infrasound sensor. For instance, some of the energy in the ~10-15 Hz band shown in the spectrogram (Figure 3f), might be related to the vibration of the infrasound sensor. It is conceivable that some of this mechanical coupling is influencing our computation of seismoacoustic cross-correlations, and coherence and phase spectrograms. Without additional infrasound sensors (and preferably less sensitive to ground motion) near VCH1, it is difficult to differentiate the volcanic processes from mechanical induced infrasound events.

561562563

564565

566

We emphasize that thanks to the infrasound detections at IS20, we can confirm that the air-to-ground coupling pattern observed at VCH1 during Stage III (Figures 3b-d) corresponds to volcanic infrasound tremor. This further supports the notion that the air-to-ground coupling pattern observed during Stage II (and similar to the one seen in Stage III) is consistent with subtle

infrasound tremor generated at the nearby fissure system. We reiterate that infrasound records, and consenquently, air-to-ground coupling observed below 7 Hz in Figure 3d should be almost or completely unaffected by mechanical vibrations of the MB2005 microbarometer.

569570571

572

573

574

575

576

577

578

579

580

567

568

Figure 5. Seismic, infrasound, and deformation time series prior to the main eruptive phase on June 26, 2018. a) Relative deformation observed inside the Sierra Negra Caldera at GPS stations GV03 and GV06 between 16:30 and 20:30. The largest displacement occurs in the vertical direction (dotted lines), but displacement is also observed in the east direction (dashed lines). Displacement is relative to the average position computed a couple hours before the main deformation which starts at ~17:40 (vertical dotted line). b) In Stage II, we record high-amplitude high-rate seismic and acoustic events at VCH1 (see also Figure 3a). Above, we display excerpts of the seismic and infrasound time series in windows of b) 10 minutes and c) 60 seconds. The beginning of the infrasound tremor (registered as air-to-ground coupled waves in Stage II; Figure 3d) coincides with the deformation onset. Vasconez et al., (2018), Bell et al., (2021a), and Bernard et al., (2022) place the beginning of the eruption ~19:40 (vertical solid line).

581 582 583

584 585 586

587

588

589

590

591

592

593

594

595

596

597

598

599

600

601

602

603

604

605

606

607

608

609

610

611

612

4.1.3 Other sources that might explain part of the air-to-ground coupling observed in Stage II

It could be possible that some of the large magnitude 4 earthquakes occurring in the caldera fault system between 17:40 and 19:40 (Figure 1a; Bell et al., 2021a) might have an infrasound component that is recorded at VCH1 as air-to-ground coupled waves. Nevertheless, we discard this mechanism to produce the observed air-to-ground coupling because these 5 individual events (Figure 1a) cannot resemble the continuous pattern we observe at VCH1 (Figures 3b-d). None of these magnitude 4 earthquakes have a detectable infrasound at IS20; we only register infrasound phases for the magnitude 5 earthquakes. Although less likely than the former option, another possibility is that infrasound from the pre-eruptive seismic tremor reported by Li et al. (2022) (Figure 1a) is travelling from the tremor epicenter and then coupling into the ground at VCH1. Matoza et al. (2009) has shown that producing observable infrasound from a seismic source that is deeper than only a few tens of meters is inefficient and unlikely to generate observable infrasound. For Mount Saint Helens, Matoza et al. (2009) show that moving a seismic source from 60 m to 195 m (below the surface) reduced the acoustic-to-seismic amplitude ratio by one order of magnitude for an observation range of 13.4 km. Here considering that the seismic tremor is mostly located at depths < 3 km (below the surface), we expect much lower amplitudes, and that the contribution of this seismic source to the overall acoustic wavefield is negligible, if not nonexistent. Furthermore, the epicenter of the seismic tremor is several kilometers (Figure 1a) away from VCH1, while the first eruptive fissure is only located a few hundred meters away, thus we expect higher attenuation from infrasound relating to seismic tremor than degassing from the nearby fissure prior to the magmatic phase. We further dismiss aforementioned mechanisms as the primary source of infrasound because the time correction required in the seismo-acoustic analysis, relating to these sources, will result in a different phase spectrogram than the one shown in Figure 3d. The back azimuths to the tremor and earthquakes epicenters differ up to 90° from our original assumption and the time correction required to achieve perfectly co-located seismic and acoustic sensors will vary. Thus, the observed coupling phases of 0° and 90° in Figure 3d will appear at angles that do not have a physical meaning and are not predicted by the theory of seismo-acoustic coupling (see Section 2.2).

4.2 Eruption onset: beginning of Stage III

We review and discuss the seismic, acoustic, and deformation signals from approximately 19:40 to 20:00 during the beginning of Stage III. Large discrete seismic events disappear and the seismic signal transitions to predominatly seismic tremor (Figure 3a). Over these 20 minutes, the energy of the seismic tremor focuses on a narrow frequency band compared to the preceding and following signals (Figure 3e). Concurrently, the frequency of the infrasound tremor progressively becomes broadband (Figure 3f). The correlogram indicates a transition from high to low frequency in the infrasound that dominates the air-to-guround coupling (Figure 3b). This frequency shift is important and might indicate the widening of the fissures close to VCH1; possibly pulsating degassing, gas jetting, and vigorous steam plumes can occur along narrow fissures, but when the activity transitions to the magmatic phase, fissures grow in size to permit the extrusion of pyroclast and gas during the lava fountain. In addition, both GV03 and GV06 indicate a small vertical movement downward, possibly indicating slight subsidence of the caldera floor (slight inflections of the vertical components around ~19:40 in Figure 5a), which may be related to magma leaving the shallow sill underneath the caldera to further feed the eruption.

4.3 Eruption migration in Sierra Negra: Stages III, IV, and V

The areas of deformation inferred from Interferometric Satellite Amplitude Radar (InSAR) imagery (Davis et al., 2021), and infrasound detections indicate magma migration through two distinct paths (Figures 4 and 6). Deformation and infrasound back azimuths show that the first path for magma migration is underneath fissures 1, 2, 3, and 6 (purple line, Figure 6), supplying magma continuously during the enterity of Stage III, from 19:40 June 26 to 16:45 June 28, 2018. We explain back azimuth variability during this first ~45 hours of the eruption (Figure 4d) as two or more fissures have been acoustically active concurrently, with the strongest infrasound source overpowering other sources at a time; this is consistent with direct observations on June 27 that show Fissures 1, 2, 3, and 6 were active simultaneously (BBC News, 2018). We further interpret back azimuth variability as magma propagating in different pulses and reaching to the surface through the fissure system. During Stage III, magma fed through the second path travels underneath Fissure 5 before 29 June (blue line in Figure 6) and sometime during Stage IV magma migrates under Fissure 4 (blue dashed line in Figure 6). Satellite detections from FIRMS (Fire Information for Resource Management System) suggest that the first thermal anomaly from Fissure 4 is on 1 July, while the volcanic acoustic energy from this fissure is only clearly detected until late 2 July 2018 at IS20 (Figure 4d). There are not clear infrasound detections from Fissure 5 as this fissure has the smallest volume of magma emplaced to surface or because the back azimuth to this fissure overlaps with the one expected for infrasound sources along Fissure 1.

We further verify that the second pathway (blue lines, Figure 6) supplied magma, during ~ 1.5 months (Stage V), to Fissure 4 and find a series of acoustic sources that have not been documented yet (Figures 6 and 7). From satellite imagery we can see that Fissure 4 (back azimuth $\sim 261.5^{\circ}$) is active throughout most of the eruption and towards 1 August the fissure propagates upslope, where the eruption ceases in late August (Figure 7). Curiously, since 5 July 2018, we register more than 1800 PMCC infrasound detections originating at back azimuth 263° (Figures 2 and 4f). This back

azimuth does not correspond to the direction of any of the fissures previously documented (Vasconez et al., 2018; Bell et al., 2021a; Bernard et al., 2022) and the large number (> 1800) of infrasound detections indicate that this back azimuth change is not due to path effects (e.g., winds; Ortiz et al., 2020; Ortiz et al., 2021) but rather to the location of new infrasound sources. From satellite imagery (Figure 7), we find persistent thermal anomalies on dates 6, 16, 23 and 28 of July located north of Fissure 4 and coincident with back azimuth of 263° (green crosses, Figure 6). One possible explanation of these scattered thermal anomalies is lava tubes skylights that have the ability to produce acoustic energy and a thermal footprint (e.g., Matoza et al., 2010). Lava tube skylights are our current best explanation for the thermal anomalies and acoustic energy; however, in-situ field mapping is pending for confirming our interpretation. Further, persistent infrasound detections from Fissure 4 and nearby acoustic sources occurred only a few hours after a 5.1 Mw earthquake, which we hypothesize indicates a second magma pulse leaving the flat-topped sill-like reservoir located ~2 km below the caldera floor (Geist et al., 2008). The co-seismic deformation indicates a subsidence of 71 cm at GV06 (Bell et al., 2021a), which is consistent with the normal faulting reported for the earthquake (Sandanbata et al., 2021). Moreover, SAR deformations between 30 June and 7 July indicate a more widespread subsidence in the southern portion of the trapdoor fault system (Shreve and Delgado, 2023), which is compatible with magma leaving the reservoir beneath the caldera and continuing to feed the flank eruption. Magma is supplied to Fissure 4 until 25 August 2018 (Bell et al., 2021a) but we only detect infrasound from the region until 18 August 2018.

Figure 6. Relevant geological features during the 2018 Sierra Negra eruption. Areas of deformation inferred from Interferometric Synthetic-Aperture Radar (InSAR) imagery (Davis et al., 2021) indicate two magma pathways (purple and blue lines). The area of deformation for the first path (purple line) remains constant between 29 June and 13 July, 2018, while the region of deformation for the second path (blue lines) indicates the advancement of magma from 29 June (continuous blue line) to 13 July (dashed blue line), 2018. Locations of 5.4 Mw earthquake (red circle) preceding the eruption at Fissure 1 and 5.1 Mw earthquake (blue circle) preceding the eruption from Fissure 4. Green crosses labeled with number 7 correspond to thermal anomalies inferred from satellite data presented in Figure 7 and consistent with infrasound observations at IS20 with back azimuth of $\sim 263^{\circ}$. Fissure numbering (1-6) after Bernard et al., (2022). The location of the seismo-acoustic station is marked with a blue triangle, whereas GPS stations are marked with blue squares. We use black dots to outline the extent of the lava flows.

Figure 7. Thermal anomalies captured in satellite imagery in the vicinity of Fissure 4. The upper left panel indicates the deformation paths shown in Figure 6 and the area enclosed in the blue square corresponds to the area shown in the subsequent subpanels. The locations of active vents of Fissure 4 are marked with blue arrows, whereas transient thermal anomalies are marked with green arrows. Only the first panel has axes in degrees, while the other panels the axes are in kilometers with respect to $[lon, lat] = [-91.22^{\circ}, -0.73^{\circ}]$.

Our infrasound detections during Stage III (the first ~45 hours of the 2018 eruption of Sierra Negra) generally agree with previous studies (Vasconez et al., 2018; Bell et al., 2021a; Bernard et al., 2022). However, infrasound observations add new information to the current knowledge of the eruption chronology, especially for estimating the order in which fissures opened and were active. Current reports of fissure activity are based from limited visual observations of the eruption or

from information gathered during field mapping campaings (Vasconez et al., 2018; Bell et al., 2021a; Bernard et al., 2022). As a result, we have found at least four different conventions for nameming the fissures in previous studies. Here, instead back azimuth and trace velocities derived at IS20 provide a more detail chronology of the fissure activity at Sierra Negra. For instance, the back azimuth and trace velocity change during the first hours can explain the migration of the eruption down the north flank, through Fissures 1, 2, 3 and 6 (Figures 4d-f and 6), and the eventual concurrent lava fountaining from these fissures. Although from direct observations we see these four fissures are eventually active altogether, we speculate that the systematic backazimuth increase $(7.55 \times 10^{-5} \, ^{\circ}/s)$, and trace velocity decrease $(-2.85 \times 10^{-4} \, m/s^2)$ between 22:54 June 26 and 12:31 June 27 (Figures 4d-e) are related to the opening of the fissures down the north flank of Sierra Negra; we assume the dominant acoustic source is accompanying this magma migration front reaching to the surface. The trace velocity decreases as the elevation of the acoustic source decreases while the eruption moves down the flank of Sierra Negra. Consequently, the incidence angle of the waveform front registered at IS20 progressively becomes shallower, resulting in a net decrease of the trace velocity. Considering the migration time inferred from infrasound and the distance between Fissures 1 and 6, the average inferred speed of the eruption migration is ~0.18 m/s or alternatively considering the average backazimuth increase rate and an approximate distance of 85 km between IS20 and the fissures, we obtain a migration speed of ~0.11 m/s. Both approaches result in similar migration speeds, but in the second approach we need to consider that the distance between IS20 and the acoustic sources does not remain constant; this can explain the small differences in both eruption migration estimates. Nevertheless, these speeds are on the same order of magnitude of magma migration inferred at Bárðarbunga in 2014 (~0.6 m/s; Sigmundsson et al., 2015) and an order of magnitude faster than the fissure propagation reported at Pu'u'Ō'ō in 2007 (~0.05 m/s; Fee et al., 2011). This is the first estimation of the migration of the eruption, which until now has not been resolved with other geophysical tools including seismicity (e.g., Bell et al, 2021a; Li et al., 2022). Further, after 12:31 June 27 and before 16:45 June 28 inferred backazimuths are variable, pointing alternately to Fissures 1, 2, 3 and 6. We interpret this back azimuth variability as energy originating from one lava fountain which overpowers the other acoustic sources; this behavior alternates between fissures. A similar competing behavior between acoustic sources was reported by Matoza et al. (2010) during the eruption of Pu'u'Ō'ō in 2007.

4.4 Back azimuth variability due to atmospheric effects.

705

706

707 708

709

710

711

712

713

714715

716

717

718

719

720

721

722

723 724

725

726

727

728

729

730

731

732

733

734

735 736 737

738

739 740

741

742743

744

745

746 747

748 749

750

Figure 8. Atmospheric profiles for air temperature (T), wind velocity (U,V), and the effective speed of sound (ceff), from 0 km to 150 km. We plot the average (solid lines) and two standard deviations (dotted lines) of hourly atmospheric profiles obtained between 19:00 June 26 and 13:00 June 27, 2018 at (-0.67, -90.74), which is the middle point between Sierra Negra and IS20. For a propagation distance of 85 km, we expect infrasound to travel mostly within the troposphere (upper limit is marked with horizontal dotted lines in blue). The lack of variation in the atmospheric profiles indicates that no significant back azimuth changes occur during infrasound propagation; instead, it suggests that back azimuth changes are related to the spatial variability of the acoustic sources.

We review atmospheric profiles of temperature, winds, and effective speed of sound between 19:00 June 26 and 13:00 June 27 to qualify backazimuth variability due to atmospheric effects.

We acquired hourly atmospheric profiles from the Ground to Space (G2S; Drob et al., 2003; Drob et al., 2010) request system (Hetzer et al., 2019). The plots showing the average and two standard deviations for air temperature, wind velocity, and effective speed of sound are presented in Figure 8, spanning from 0 km to 150 km. Since the propagation distance is 85 km, we only expect arrivals from the troposphere. At tropospheric altitudes (< 15 km), we find that atmospheric profiles almost remain unchanged over the first 18 hours of the eruption, when the eruption started at Fissure 1 and then progressively migrated down the north flank of Sierra Negra. Geographically, the first segment of Fissure 1 is located at back azimuth 256.7°, only 0.3° off from our average back azimuth of 257° inferred from IS20 between 19:45 and 22:54 on June 26 (Figure 4); during this ~3 hours our back azimuth estimates have a very small scatter (0.4° for one standard deviation), which is consistent with the almost constant atmospheric specifications.

We also benchmark our back azimuth estimates for the two major earthquakes of moment magnitudes 5.4 and 5.1 on 09:15 June 26 and 00:30 July 5, respectively. Both earthquakes are closely located (Figures 1a and 6) at geographical backazimuth of ~253°, which is only 0.2° off from our infrasound inferred backazimuths of 252.8° at IS20. Epicentral infrasound is a well-documented phenomenon that is often accompanied by other infrasound phases (e.g., Mutschlecner and Whitaker, 2005; Arrowsmith et al., 2010; Johnson et al., 2020; Fee et al., 2023). These phases could be related to secondary or local infrasound generated by the passage of the earthquakes' surface waves interacting with topography. According to Mutschlecner and Whitaker (2005) these additional phases can precede or follow the infrasound signals from the earthquake epicenter.

All these observations between infrasound and geographical inferred back azimuths suggest that atmospheric variability does not add a large uncertainty to our observations. However, it is possible that for other time periods, besides the ones discussed in this section, atmospheric variability adds a significant uncertainty to our back azimuth estimates of the Sierra Negra eruption. Further, CRB error estimates on back azimuth quantification appear to be closer to our observational uncertainties (~0.3°) than those predicted by Szuberla and Olson (2004).

Considering that the acoustic source is close to zero altitude (~90-1000 m asl), there is not a clear duct in the troposphere (Figure 8) that would facilitate infrasound propagation from Sierra Negra to IS20. Thus, ray theory is limited in studying the effects that infrasound waves undergo along the propagation path. It is also possible that diffraction of the acoustic wavefield, which is not captured by the ray theory, is significant in this propagation context. Normal mode or parabolic equation simulations (Waxler and Assink, 2019 and references therein) would be the next step to investigate the atmospheric propagation path from Sierra Negra to IS20, but are beyond the scope of the present work. Nevertheless, the relative temporal stability of the atmospheric profiles (Figure 8) supports our inference that atmospheric variability is not driving the observed back azimuth changes.

4.5 Summary of new observations of the 2018 Sierra Negra eruption.

Stage I (09:15-17:40 June 26): Although the seismicity and deformation provide in better detail the evolution of Sierra Negra for the hours preceding the eruption, we show that the large 5.4 Mw earthquake can be detected at IS20 (Figures 4 d and f) and subtle coupling is observed at VCH1

from 13:00 to 16:30 (Figures 3c-d), possibly related to the mechanical shaking of the MB2005 microbarometer coincident with increased seismicity.

Stage II (17:40-19:40 June 26): Precursory air-to-ground coupling is detected at VCH1 and is indicative of infrasound tremor generated at the nearby fissures. The infrasound tremor is consistent with an air-to-ground source; therefore, a purely seismic model cannot be used (e.g., Li et al., 2022). Instead, it is consistent with surface activity that could be explained through pulsating degassing, gas jetting, and vigorous steam plumes. The apparent differences between the purely seismic model provide by Li et al. (2022) and our acoustic observations could be due to the uncoupled seismic generation at depth with infrasound generation at surface or to weak seismic process that are challenging to retrive from the seismic signal because of the concurrent high-rate, high-amplitude seismic events. Furthermore, ambiguity remains on interpreting some of the seismic and infrasound features we observe in this stage. For instance, seismic spectral lines and gliding might be related to the well-know "Dirac comb" effect or to changes in the site and path responses. As for the infrasound data, it is possible that at high-frequencies (> 7 Hz) the records might be contaminated by mechanical vibrations of the microbarometer.

Stage III (19:40 June 26 – 16:45 June 28): In contrast to what was initially reported by Vasconez et al. (2018) and then repeated in subsequent estudies (e.g., Davis et al., 2021; Shreve and Delgado, 2023), the eruption at Fissures 1, 2, 3, and 6 lasted for more than 24 hours as infrasound detections at IS20 (Figure 4d) indicate continous activity from these fissures during the entire stage (~45 h). At the beginning of this stage, from 19:40 to 20:00 on June 26, seismo-acoustic analysis (Figure 3b) shows that infrasound that dominates air-to-ground coupling transitions from high- to low-frequencies, possibly associated with the wideing of the eruptive fissures as the magmatic phase starts. Moreover, between 19:45 and 22:54 on June 26, persistent infrasound detections at IS20 indicate acoustic sources at back azimuth 257° (Figures 4d and 4f, numeric labels 2-3), which suggests that the region where Fissure 1 intersects the caldera rim was first to rupture and erupt. Later, from 22:54 June 26 to 12:31 June 27 (Figures 4d-e), we infer that the eruption migration down the flank of Sierra Negra occurs at a rate of 0.11-0.18 m/s with two or more fissures being acoustically active.

Stage IV (16:45 June 28 - 00:29 July 05): This period is charactized by nearly acoustic quiescence. The near-infra red satellite observations indicate that Fissure 4 was not active on June 30 (Figure 7) and on FIRMS, thermal anomalies close to the fissure are first detected on July 1. We do not detect acoustic energy from the region close to Fissure 4 until late July 2 (Figure 4d). It is possible that low-energy acoustic emissions from Fissure 4 in July 1 are not detected at IS20 as these emissions might have been attenuated by the atmosphere during propagation. The other possibility is that, given the coarse spatial resolution of the thermal alerts, the detection on July 1 is a false positive, maybe related to a lava flow from another fissure or a processing artifact.

Stage V (00:30 July 05 – 00:00 August 19): The acoustic component of the 5.1 Mw earthquake is detected at IS20 and followed by incessant infrasound detections from the region close to Fissure 4. The infrasound detections extended until August 18 and coincided with our last near-infrared satellite image confirming the continued activity of Fissure 4 (Figure 7). Nevertheless, the eruption was reported to end on August 25 (e.g., Vasconez et al., 2018; Bell et al., 2021a; Bernard et al., 2022). The majority of the detections are located at back azimuth of ~263°, which is approximately

a 1.5° difference from where Fissure 4 is located. The 263° back azimuth, instead, is consistent with multiple thermal anomalies (Figure 6 and 7) that might indicate acoustic activity from lava tube skylights.

5 Conclusions

By analyzing data from VCH1, a single seismo-acoustic station, located in proximity (~0.4 km) to the eruptive fissures and IS20, an infrasound array located ~85 kilometers from the volcano, we provide new insights into the eruption sequence of Sierra Negra in 2018. Specifically, seismoacoustic analysis (Figure 3) reveals infrasound tremor, starting at 17:40 on June 26 about 2 hours before the current official eruption onset time (~19:40 June 26) for the 2018 Sierra Negra eruption. In addition, we demonstrate that infrasound can capture the eruption migration along the north flank at unprecedent temporal and spatial resolutions. The magma migration occurred over two distinct pathways (Figure 6), which were activate sequentially. The first magma pathway was active between 19:40 June 26 and 16:45 June 28 and fed the Fissures 1, 2, 3 and 6 (Figure 4). From the infrasound records, we infer that the magma front migrated beneath Fissures 1, 2, 3 and 6 at a rate of 0.11-0.18 m/s and that two or more fissures were acoustically active simultaneously; with the most energetic acoustic source overpowering acoustic emissions from the other fissures. The second pathway fed Fissure 4 (the most distal fissure to the caldera rim), Fissure 5, and acoustic sources detected at back azimuth 263°. The 263° back azimuth does not coincide with previously mapped fissures, but it is consistent with lava flow mapping, persistent thermal anomalies, and coeruptive deformation derived from InSAR. These geological features appear to be lava tube skylights which until now have not been documented in the area and an in-situ field campaign is needed to investigate this hypothesis.

Acknowledgments

We would like to thank Toshiro Tanimoto and Chen Ji, who provided feedback during this project. We thank Paola García from the Chilean National Data Center of the CTBTO and also thank Andrew Bell and one anonymous reviewer for their thoughtful and constructive suggestions. This work was funded by NSF grants EAR-1847736 and EAR-1620576. The views expressed herein are those of the authors and do not necessarily reflect the views of the CTBTO Preparatory Commission.

Open Research

Raw cGPS data are available through the UNAVCO archive at (Geist et al., 2002). Also parsed cGPS data are openly available from the Nevada Geodetic Lab (Blewitt et al., 2018). Parsed InSAR data are available from (Davis et al., 2021). Seismo-acoustic data from VCH1 are available at the Ecuadorian national network through of the Instituto Geofisico, Escuela Politécnica Nacional request system (IGEPN, 2024). All data from the International Monitoring System are available for scientific studies through the CTBTO Virtual Data Exploration Centre (VDEC, 2024). Visual and near-infrared satallite imagery used in this study are available at (Ortiz et al., 2024). Atmospheric profiles can be requested at (Hetzer et al., 2019).

References

- Alcoverro, B., Martysevich, P., & Starovoit, Y. (2005). Mechanical sensitivity of microbarometers
- MB2000 (DASE, France) and Chaparral 5 (USA) to vertical and horizontal ground motion.
- 892 Inframatics, 9, 1-10.

893

- Alvarado, A., Ruiz, M., Mothes, P., Yepes, H., Segovia, M., Vaca, M., et al. (2018). Seismic,
- 895 volcanic, and geodetic networks in Ecuador: Building capacity for monitoring and research.
- 896 Seismological Research Letters, 89(2A), 432–439. https://doi.org/10.1785/0220170229

897

- Anthony R. E. Watzak J. Ringler A. T., and Wilson D. C. 2022. Characteristics, relationships, and
- precision of direct acoustic-to-seismic coupling measurements from local explosions, Geophys. J.
- 900 Int. 230, no. 3, 2019–2035, doi: https://doi.org/10.1093/gji/ggac154.

901

- Amelung, F., Jónsson, S., Zebker, H. et al. Widespread uplift and 'trapdoor' faulting on Galápagos
- 903 volcanoes observed with radar interferometry. Nature 407, 993–996 (2000).
- 904 https://doi.org/10.1038/35039604

905

- Anguita, F., & Hernán, F. (2000). The Canary Islands origin: a unifying model. Journal of
- 907 Volcanology and Geothermal Research, 103(1-4), 1-26.

908

- Arrowsmith, S. J., Johnson, J. B., Drob, D. P., & Hedlin, M. A. (2010). The seismoacoustic
- wavefield: A new paradigm in studying geophysical phenomena. Reviews of Geophysics, 48(4).

911

- 912 BBC News (2018). Galapagos' Sierra Negra volcano eruption triggers evacuation
- 913 https://www.bbc.com/news/world-latin-america-44627725

914

- Barrière, J., Oth, A., d'Oreye, N., Subira, J., Smittarello, D., Brenot, H., Theys, N. and Smets, B.,
- 2023. Local Infrasound Monitoring of Lava Eruptions at Nyiragongo Volcano (DR Congo) Using
- 917 Urban and Near-Source Stations. Geophysical Research Letters, 50(18), p.e2023GL104664.

918

- Bell, A.F., La Femina, P.C., Ruiz, M. et al. Caldera resurgence during the 2018 eruption of Sierra
- 920 Negra volcano, Galápagos Islands. Nat Commun 12, 1397 (2021a).
- 921 https://doi.org/10.1038/s41467-021-21596-4

922

- Bell, A. F., Hernandez, S., La Femina, P. C., & Ruiz, M. C. (2021b). Uplift and seismicity driven
- 924 by magmatic inflation at Sierra Negra volcano, Galápagos Islands. Journal of Geophysical
- 925 Research: Solid Earth, 126, e2021JB022244. https://doi.org/10.1029/2021JB022244

926

927 Ben-Menahem, A., and S. J. Singh (1981), Seismic Waves and Sources, Springer, New York.

928

- 929 Bernard, B., Ramón, P., García, L., Hernandez, S., Vasconez, F. J., Viracucha, G. and Hidalgo, S.
- 930 (2022) "Volcanic event management in the Galápagos Islands, Ecuador", Volcanica, 5(1), pp.
- 931 209–225. doi: 10.30909/vol.05.01.209225.

- Bishop, J. W., Haney, M. M., Fee, D., Matoza, R. S., McKee, K. F., & Lyons, J. J. (2023). Back-933
- 934 Azimuth Estimation of Air-to-Ground Coupled Infrasound from Transverse Coherence
- Minimization. The Seismic Record, 3(4), 249-258. 935

- Blewitt, G., Hammond, W. C., and Kreemer, C. (2018), Harnessing the GPS data explosion for 937
- interdisciplinary science, Eos, 99, https://doi.org/10.1029/2018EO104623. Published on 24 938
- 939 September 2018.

940

- Cansi, Y. (1995). An automatic seismic event processing for detection and location: The P.M.C.C. 941
- 942 method. Geophysical Research Letters, 22(9), 1021–1024. https://doi.org/10.1029/95GL00468

943

- Carracedo, J. C. (1994). The Canary Islands: an example of structural control on the growth of 944
- large oceanic-island volcanoes. Journal of Volcanology and Geothermal Research, 60(3-4), 225-945
- 241. 946

947

948 CEA-Martec (2007). MB2005 user manual.

949

CEA (2016). Dase Tool Kit, User Manual, version 5.5 950

951

- 952 Chadwick, W. W., & Howard, K. A. (1991). The pattern of circumferential and radial eruptive
- fissures on the volcanoes of Fernandina and Isabela islands, Galapagos. Bulletin of Volcanology, 953
- 53, 259-275. 954

955

- Davis, T., Bagnardi, M., Lundgren, P., & Rivalta, E. (2021). Extreme curvature of shallow 956
- magma pathways controlled by competing stresses: Insights from the 2018 Sierra Negra 957
- 958 eruption. Geophysical Research Letters, 48,
- 2021GL093038. https://doi.org/10.1029/2021GL093038 959

960

- Dieterich, J. H. (1988). Growth and persistence of Hawaiian volcanic rift zones. Journal of 961
- Geophysical Research: Solid Earth, 93(B5), 4258-4270. 962

963

- 964 Drob, D. P., Picone, J. M., & Garcés, M. (2003). Global morphology of infrasound propagation.
- 965 Journal of Geophysical Research: Atmospheres, 108(D21).

966

- Drob, D.P., Garcés, M., Hedlin, M., and Brachet, N. (2010). The temporal morphology of 967
- infrasound propagation. Pure and Applied Geophysics 167 (4-5), 437-453. doi:10.1007/s00024-968
- 010-0080-6. 969

970

- 971 Fee, D., and M. Garcés (2007), Infrasonic tremor in the diffraction zone, Geophys. Res. Lett., 34,
- L16826, doi:10.1029/2007GL030616. 972

973

- Fee, D., Garces, M., & Steffke, A. (2010). Infrasound from Tungurahua volcano 2006–2008: 974
- Strombolian to Plinian eruptive activity. Journal of Volcanology and Geothermal Research, 193(1-975
- 976 2), 67-81.

- Fee, D., Garces, M., Orr, T., and Poland, M. (2011), Infrasound from the 2007 fissure eruptions
- 979 of Kīlauea Volcano, Hawai'i, Geophys. Res. Lett., 38, L06309, doi:10.1029/2010GL046422.
- 980
- Fee, D., and R.S. Matoza (2013), An overview of volcano infrasound: from hawaiian to plinian,
- local to global, J. Volcanol. Geotherm. Res., 249, 123-139, doi:10.1016/j.jvolgeores.2012.09.002
- 983
- Fee, D., Macpherson, K., & Gabrielson, T. (2023). Characterizing infrasound station frequency
- 985 response using large earthquakes and colocated seismometers. Bulletin of the Seismological
- 986 Society of America.

- 988 Garcés, M., Harris, A., Hetzer, C., Johnson, J., Rowland, S., Marchetti, E., and Okubo,
- 989 P. (2003), Infrasonic tremor observed at Kīlauea Volcano, Hawai'i, Geophys. Res. Lett., 30,
- 990 2023, doi:10.1029/2003GL018038, 20.

991

- 992 Geist, D., Chadwick, B. W., Meertens, C. (2002) Galapagos GPS Network GV03-GV03 P.S.,
- 993 The GAGE Facility operated by EarthScope Consortium, GPS/GNSS Observations Dataset
- 994 [Dataset], https://doi.org/10.7283/T5N58JM5.

995

- 996 Geist, D., Chadwick, B. W., Meertens, C. (2002) Galapagos GPS Network GV06-GV06 P.S.,
- 997 The GAGE Facility operated by EarthScope Consortium, GPS/GNSS Observations Dataset
- 998 [Dataset], https://doi.org/10.7283/T5M61HHS.

999

- 1000 Geist, D.J., Harpp, K.S., Naumann, T.R. et al. The 2005 eruption of Sierra Negra volcano,
- 1001 Galápagos, Ecuador. Bull Volcanol 70, 655–673 (2008). https://doi.org/10.1007/s00445-007-
- 1002 0160-3

1003

- Gestrich, J. E., Fee, D., Matoza, R. S., Lyons, J. J., Dietterich, H. R., Cigala, V., ... & Parcheta, C.
- 1005 E. (2022). Lava fountain jet noise during the 2018 eruption of fissure 8 of Kīlauea volcano.
- Frontiers in Earth Science, 10, 1027408.

1007

- 1008 Gordeev, E. (1993). Modeling of volcanic tremor as explosive point sources in a single-layered,
- elastic half-space. Journal of Geophysical Research: Solid Earth, 98(B11), 19687-19703.

1010

- Gregg, P. M., Zhan, Y., Amelung, F., Geist, D., Mothes, P., & Koric, S. (2022). Forecasting
- mechanical failure and the 26 June 2018 eruption of Sierra Negra Volcano, Galápagos. Ecuador
- 1013 Sci Adv, 8(22), 1-9.

1014

- Hagerty, M. T., Schwartz, S. Y., Garces, M. A., & Protti, M. (2000). Analysis of seismic and
- acoustic observations at Arenal Volcano, Costa Rica, 1995–1997. Journal of Volcanology and
- 1017 Geothermal Research, 101(1-2), 27-65.

1018

- 1019 Hetzer, C.H., Drob, D.P., and Zabel, K. (2019). The NCPA-G2S request system.
- https://g2s.ncpa.olemiss.edu. Accessed 2024-08-15

- Hibert, C., Mangeney, A., Polacci, M., Muro, A. D., Vergniolle, S., Ferrazzini, V., ... & Lauret, F.
- 1023 (2015). Toward continuous quantification of lava extrusion rate: Results from the multidisciplinary

- analysis of the 2 January 2010 eruption of Piton de la Fournaise volcano, La Réunion. Journal of
- Geophysical Research: Solid Earth, 120(5), 3026-3047
- 1026
- Hjartardóttir, Á. R., Dürig, T., Parks, M., Drouin, V., Eyjólfsson, V., Reynolds, H., ... & Pedersen,
- 1028 G. B. (2023). Pre-existing fractures and eruptive vent openings during the 2021 Fagradalsfjall
- eruption, Iceland. Bulletin of Volcanology, 85(10), 56.

- Houghton, B. F., Tisdale, C. M., Llewellin, E. W., Taddeucci, J., Orr, T. R., Walker, B. H., &
- Patrick, M. R. (2021). The birth of a Hawaiian fissure eruption. Journal of Geophysical Research:
- 1033 Solid Earth, 126(1), e2020JB020903.

1034

- Hotovec, A. J., Prejean, S. G., Vidale, J. E., & Gomberg, J. (2013). Strongly gliding harmonic
- tremor during the 2009 eruption of Redoubt Volcano. Journal of Volcanology and Geothermal
- 1037 Research, 259, 89-99.

1038

- Hotovec-Ellis, A. J., Shiro, B. R., Shelly, D. R., Anderson, K. R., Haney, M. M., Thelen, W. A.,
- 1040 ... & Johanson, I. A. (2022). Earthquake-derived seismic velocity changes during the 2018 caldera
- 1041 collapse of Kīlauea volcano. Journal of Geophysical Research: Solid Earth, 127(2),
- 1042 e2021JB023324.

1043

- 1044 Ichihara, M., Takeo, M., Yokoo, A., Oikawa, J., & Ohminato, T. (2012). Monitoring volcanic
- activity using correlation patterns between infrasound and ground motion. Geophysical Research
- 1046 Letters, 39(4).

1047

- 1048 Ichihara, M. (2016). Seismic and infrasonic eruption tremors and their relation to magma discharge
- rate: A case study for sub-Plinian events in the 2011 eruption of Shinmoe-dake, Japan. Journal of
- Geophysical Research: Solid Earth, 121(10), 7101-7118.

1051

- 1052 Ichihara, M., Yamakawa, K., & Muramatsu, D. (2021). A simple method to evaluate the air-to-
- ground coupling efficiency: a tool helping the assessment of seismic/infrasonic energy partitioning
- during an eruption. Earth, Planets and Space, 73, 1-9.

1055

- 1056 IGEPN, 2024, Instituto Geofísico Escuela Politécnica Nacional, data download system [Dataset],
- 1057 https://www.igepn.edu.ec/senales-sismicas/estaciones-en-formato-mseed

1058

- Johnson, J. B., & Aster, R. C. (2005). Relative partitioning of acoustic and seismic energy during
- Strombolian eruptions. Journal of Volcanology and Geothermal Research, 148(3-4), 334-354.

1061

- Johnson, J. B., & Ripepe, M. (2011). Volcano infrasound: A review. Journal of Volcanology and
- 1063 Geothermal Research, 206(3-4), 61-69.

1064

- Johnson, J. (2019). Local volcano infrasound monitoring. Infrasound Monitoring For Atmospheric
- Studies: Challenges In Middle Atmosphere Dynamics And Societal Benefits, 989-1022.

- Johnson, J. B., Mikesell, T. D., Anderson, J. F., & Liberty, L. M. (2020). Mapping the sources of
- proximal earthquake infrasound. Geophysical Research Letters, 47(23), e2020GL091421.

Jónsson, S., Zebker, H., & Amelung, F. (2005). On trapdoor faulting at Sierra Negra volcano, Galápagos. Journal of Volcanology and Geothermal Research, 144(1-4), 59-71.

1073

Lai, V. H., Zhan, Z., Brissaud, Q., Sandanbata, O., & Miller, M. S. (2021). Inflation and asymmetric collapse at Kīlauea summit during the 2018 eruption from seismic and infrasound analyses. Journal of Geophysical Research: Solid Earth, 126(10), 2021JB022139.

1077

Li, K. L., Bean, C. J., Bell, A. F., Ruiz, M., Hernandez, S., & Grannell, J. (2022). Seismic tremor reveals slow fracture propagation prior to the 2018 eruption at Sierra Negra volcano, Galápagos. Earth and Planetary Science Letters. https://doi.org/10.1016/j.epsl.2022.117533.

1081

Lyons, J.J., Dietterich, H.R., Patrick, M.P. et al. High-speed lava flow infrasound from Kīlauea's fissure 8 and its utility in monitoring effusion rate. Bull Volcanol 83, 66 (2021). https://doi.org/10.1007/s00445-021-01488-7

1085

Marchetti, E., Ripepe, M., Campus, P. et al. Long range infrasound monitoring of Etna volcano. Sci Rep 9, 18015 (2019). https://doi.org/10.1038/s41598-019-54468-5

1088

Matoza, R.S., M.A. Garces, B.A. Chouet, L. D'Auria, M.A.H. Hedlin, C. De Groot-Hedlin, and G.P. Waite (2009), The source of infrasound associated with long-period events at Mount St. Helens, J. Geophys. Res., 114, B04305, doi:10.1029/2008JB006128

1092

Matoza, R. S., Fee, D., and Garcés, M. A. (2010), Infrasonic tremor wavefield of the Pu'u 'Ō'ō crater complex and lava tube system, Hawaii, in April 2007, J. Geophys. Res., 115, B12312, doi:10.1029/2009JB007192

1096

Matoza, R. S., Le Pichon, A., Vergoz, J., Herry, P., Lalande, J. M., Lee, H. I., ... & Rybin, A. (2011). Infrasonic observations of the June 2009 Sarychev Peak eruption, Kuril Islands: Implications for infrasonic monitoring of remote explosive volcanism. Journal of Volcanology and Geothermal Research, 200(1-2), 35-48.

1101

Matoza, R. S., M., Landès, A., Le Pichon, L., Ceranna, and D., Brown (2013), Coherent ambient infrasound recorded by the International Monitoring System, Geophys. Res. Lett., 40, 429–433, doi:10.1029/2012GL054329.

1105

Matoza, R. S., & Fee, D. (2014). Infrasonic component of volcano-seismic eruption tremor. Geophysical Research Letters, 41(6), 1964-1970.

1108

Matoza, R. S., Fee, D., Green, D. N., Le Pichon, A., Vergoz, J., Haney, M. M., ... & Ceranna, L. (2018). Local, regional, and remote seismo-acoustic observations of the April 2015 VEI 4 eruption of Calbuco volcano, Chile. Journal of Geophysical Research: Solid Earth, 123(5), 3814-3827.

- 1113 Matoza, R.S., D. Fee, J.D. Assink, A.M. Iezzi, D.N. Green, K. Kim, L. Toney, T. Lecocq, S.
- Krishnamoorthy, J.-M. Lalande, K. Nishida, K.L. Gee, M.M. Haney, H.D. Ortiz, Q. Brissaud, L.
- 1115 Martire, L. Rolland, P. Vergados, A. Nippress, J. Park, S. Shani-Kadmiel, A. Witsil, S.

- Arrowsmith, C. Caudron, S. Watada, A.B. Perttu, B. Taisne, P. Mialle, A. Le Pichon, J. Vergoz,
- P. Hupe, P.S. Blom, R. Waxler, S. De Angelis, J.B. Snively, A.T. Ringler, R.E. Anthony, A.D.
- Jolly, G. Kilgour, G. Averbuch, M. Ripepe, M. Ichihara, A. Arciniega-Ceballos, E. Astafyeva, L.
- 1119 Ceranna, S. Cevuard, I.-Y. Che, R. De Negri, C.W. Ebeling, L.G. Evers, L.E. Franco-Marin, T.B.
- Gabrielson, K. Hafner, R.G. Harrison, A. Komjathy, G. Lacanna, J. Lyons, K.A. Macpherson, E.
- Marchetti, K.F. McKee, R.J. Mellors, G. Mendo-Pérez, T.D. Mikesell, E. Munaibari, M. Oyola-
- Merced, I. Park, C. Pilger, C. Ramos, M.C. Ruiz, R. Sabatini, H.F. Schwaiger, D. Tailpied, C.
- Talmadge, J. Vidot, J. Webster, D.C. Wilson (2022), Atmospheric waves and global
- seismoacoustic observations of the January 2022 Hunga eruption, Tonga, Science, 377, 6601, 95-
- 1125 100, doi:10.1126/science.abo7063
- 1126
- 1127 Matoza, R. S., & Roman, D. C. (2022). One hundred years of advances in volcano seismology and
- acoustics. Bulletin of Volcanology, 84(9), 86.
- 1129
- 1130 McKee, K., D. Fee, M. Haney, R.S. Matoza, and J. Lyons (2018), Infrasound signal detection and
- back azimuth estimation using ground-coupled airwaves on a seismo-acoustic sensor pair, J.
- Geophys. Res. Solid Earth, 123, 6826-6844, doi:10.1029/2017JB015132
- 1133
- McKee, K., Fee, D., Yokoo, A., Matoza, R. S., & Kim, K. (2017). Analysis of gas jetting and
- fumarole acoustics at Aso Volcano, Japan. Journal of Volcanology and Geothermal Research, 340,
- 1136 16-29.
- 1137
- McKee K, Smith CM, Reath K, Snee E, Maher S, Matoza RS, Carn S, Mastin L, Anderson K,
- Damby D, Roman DC, Degterev A, Rybin A, Chibisova M, Assink JD, de NegriLeiva R, Perttu
- 1140 A (2021) Evaluating the state-of-the-art in remote volcanic eruption characterization Part I:
- 1141 Raikoke volcano Kuril Islands. J Volcanol Geotherm Res.
- https://doi.org/10.1016/j.jvolgeores.2021.107354
- 1143
- Merchant, B. J., & McDowell, K. D. (2014). MB3a Infrasound Sensor Evaluation (No.
- SAND2014-20108). Sandia National Lab.(SNL-NM), Albuquerque, NM (United States).
- 1146
- Muramatsu, D., Ichihara, M., Matsushima, T., Kuwano, O., & Tajima, Y. (2022). Surface eruptive
- dynamics of 2018 small phreatic eruption of Iwo-Yama volcano, Japan: Constraints from seismo-
- acoustic observation and mud suspension rheology. Journal of Volcanology and Geothermal
- 1150 Research, 421, 107452.
- 1151
- Mutschleener, J. P., & Whitaker, R. W. (2005). Infrasound from earthquakes. Journal of
- Geophysical Research: Atmospheres, 110(D1).
- 1154
- Nief, G., Talmadge, C., Rothman, J., & Gabrielson, T. (2019). New generations of infrasound
- sensors: technological developments and calibration. Infrasound Monitoring for Atmospheric
- Studies: Challenges in Middle Atmosphere Dynamics and Societal Benefits, 63-89
- 1158
- Nishida, K., & Ichihara, M. (2016). Real-time infrasonic monitoring of the eruption at a remote
- island volcano using seismoacoustic cross correlation. Geophysical Journal International, 204(2),
- 1161 748-752.

- Ortiz, H. D., Matoza, R. S., Garapaty, C., Rose, K., Ramón, P., & Ruiz, M. C. (2020). Multi-year
- regional infrasound detection of Tungura- hua, El Reventador, and Sangay volcanoes in Ecuador
- from 2006 to 2013. Proceedings of Meetings on Acoustics, 41, 022003. https://doi.
- 1166 org/10.1121/2.0001362

1167

- Ortiz, H. D., Matoza, R. S., Johnson, J. B., Hernandez, S., Anzieta, J. C., & Ruiz, M. C. (2021).
- Autocorrelation infrasound interferometry. Journal of Geophysical Research: Solid Earth, 126(4),
- e2020JB020513. https://doi.org/10.1029/2020JB020513

1171

- Ortiz, H., Matoza, R., Bernard, B., De Negri, R., and Ruiz, M. (2024). Satellite data of the 2018
- 1173 Sierra Negra eruption in the Galápagos Islands [Dataset]. Dryad.
- https://doi.org/10.5061/dryad.wstqjq2w5

1175

- Palacios, P. B., Díez, M., Kendall, J. M., & Mader, H. M. (2016). Seismic-acoustic energy
- partitioning during a paroxysmal eruptive phase of Tungurahua volcano, Ecuador. Geophysical
- 1178 Journal International, 205(3), 1900-1915.

1179

- Patrick, M. R., Dietterich, H. R., Lyons, J. J., Diefenbach, A. K., Parcheta, C., Anderson, K. R., ...
- & Kauahikaua, J. P. (2019). Cyclic lava effusion during the 2018 eruption of Kīlauea Volcano.
- 1182 Science, 366(6470), eaay9070.

1183

- Peltier, A., Chevrel, M.O., Harris, A.J.L. et al. Reappraisal of gap analysis for effusive crises at
- Piton de la Fournaise. J Appl. Volcanol. 11, 2 (2022). https://doi.org/10.1186/s13617-021-00111-
- 1186 w

1187

- Perttu, A., J. Assink, A. R. Van Eaton, C. Caudron, C. Vagasky, J. Krippner, K. McKee, S. De
- Angelis, B. Perttu, B. Taisne, et al. (2023). Remote Characterization of the 12 January 2020
- 1190 Eruption of Taal Volcano, Philippines, Using Seismo-Acoustic, Volcanic Lightning, and Satellite
- 1191 Observations. Bulletin of the Seismological Society of America 2023; doi:
- 1192 https://doi.org/10.1785/0120220223

1193

- Powell, T. W., & Neuberg, J. (2003). Time dependent features in tremor spectra. Journal of
- Volcanology and Geothermal Research, 128(1-3), 177-185.

1196

- Ripepe, M., Marchetti, E., Delle Donne, D., Genco, R., Innocenti, L., Lacanna, G., & Valade,
- 1198 S. (2018). Infrasonic early warning system for explosive eruptions. Journal of Geophysical
- 1199 Research: Solid Earth, 123, 9570–9585. https://doi.org/10.1029/2018JB015561

1200

- Ruiz, M. Z., Civilini, F., Ebinger, C. J., Oliva, S. J., Ruiz, M. C., Badi, G., La Femina, P. C., &
- 1202 Casas, J. A. (2022). Precursory signal detected for the 2018 Sierra Negra Volcanic Eruption,
- Galápagos, using seismic ambient noise. Journal of Geophysical Research: Solid Earth, n/a(n/a),
- e2021JB022990. https://doi.org/10.1029/2021JB022990

- Sandanbata, O., Kanamori, H., Rivera, L., Zhan, Z., Watada, S., & Satake, K. (2021). Moment
- tensors of ring-faulting at active volcanoes: Insights into vertical-CLVD earthquakes at the Sierra

- Negra caldera, Galápagos Islands. Journal of Geophysical Research: Solid Earth, 126(6),
- 1209 e2021JB021693.
- 1210
- 1211 Sciotto, M., Watson, L.M., Cannata, A. et al. Infrasonic gliding reflects a rising magma column at
- Mount Etna (Italy). Sci Rep 12, 16954 (2022). https://doi.org/10.1038/s41598-022-20258-9
- 1213
- 1214 Shreve, T., & Delgado, F. (2023). Trapdoor fault activation: A step toward caldera collapse at
- 1215 Sierra Negra, Galápagos, Ecuador. Journal of Geophysical Research: Solid Earth, 128(5),
- 1216 e2023JB026437.

- 1218 Sigmundsson, F., Hooper, A., Hreinsdóttir, S. et al. Segmented lateral dyke growth in a rifting
- 1219 event at Bárðarbunga volcanic system, Iceland. Nature 517, 191-195 (2015).
- 1220 https://doi.org/10.1038/nature14111

1221

- Spina, L., Cannata, A., Morgavi, D., Privitera, E., & Perugini, D. (2022). Seismo-acoustic gliding:
- An experimental study. Earth and Planetary Science Letters, 579, 117344.
- Thelen, W., Waite, G., Lyons, J. et al. Infrasound observations and constraints on the 2018
- eruption of Kīlauea Volcano, Hawaii. Bull Volcanol 84, 76 (2022)
- 1226 https://doi.org/10.1007/s00445-022-01583-3

1227

- Szuberla, C. A., & Olson, J. V. (2004). Uncertainties associated with parameter estimation in
- atmospheric infrasound arrays. The Journal of the Acoustical Society of America, 115(1), 253-
- 1230 258.

1231

- Thelen, W., Waite, G., Lyons, J., & Fee, D. (2022). Infrasound observations and constraints on the
- 2018 eruption of Kīlauea Volcano, Hawaii. Bulletin of Volcanology, 84(8), 76.

1234

1235 Tilling, R. I., & Dvorak, J. J. (1993). Anatomy of a basaltic volcano. Nature, 363(6425), 125-133.

1236

- Vasconez, F. J., Ramón, P., Hernandez, S., Hidalgo, S., Bernard, B., Ruiz, M., Alvarado, A., La
- Femina, P. and Ruiz, G. (2018) "The different characteristics of the recent eruptions of Fernandina
- and Sierra Negra volcanoes (Galápagos, Ecuador)", Volcanica, 1(2), pp. 127–133. doi:
- 1240 10.30909/vol.01.02.127133.

1241

- 1242 VDEC (2024). Virtual Data Exploration Centre [Dataset], https://www.ctbto.org/resources/for-
- 1243 researchers-experts/vdec

1244

- Watson, L. M., Iezzi, A. M., Toney, L., Maher, S. P., Fee, D., McKee, K., ... & Johnson, J. B.
- 1246 (2022). Volcano infrasound: progress and future directions. Bulletin of Volcanology, 84(5), 44.

1247

- Waxler, R., & Assink, J. (2019). Propagation modeling through realistic atmosphere and
- benchmarking. Infrasound monitoring for atmospheric studies: Challenges in middle atmosphere
- dynamics and societal benefits, 509-549.

- 1252 Yamakawa, K., Ichihara, M., Muramatsu, D., Matsushima, T., Takahashi, H., Wada, R., &
- Shimoyama, I. (2023). Experiment to distinguish two fumaroles consistently emanating infrasound
- at Kirishima Iwo-Yama. earth, planets and space, 75(1), 26.
- 1255
- Yun, S., Segall, P., & Zebker, H. (2006). Constraints on magma chamber geometry at Sierra Negra
- volcano, Galápagos islands, based on InSAR observations. Journal of Volcanology and
- Geothermal Research, 150(1), 232–243. https://doi.org/10.1016/j.jvolgeores.2005.07.009

Figure	1.
--------	----

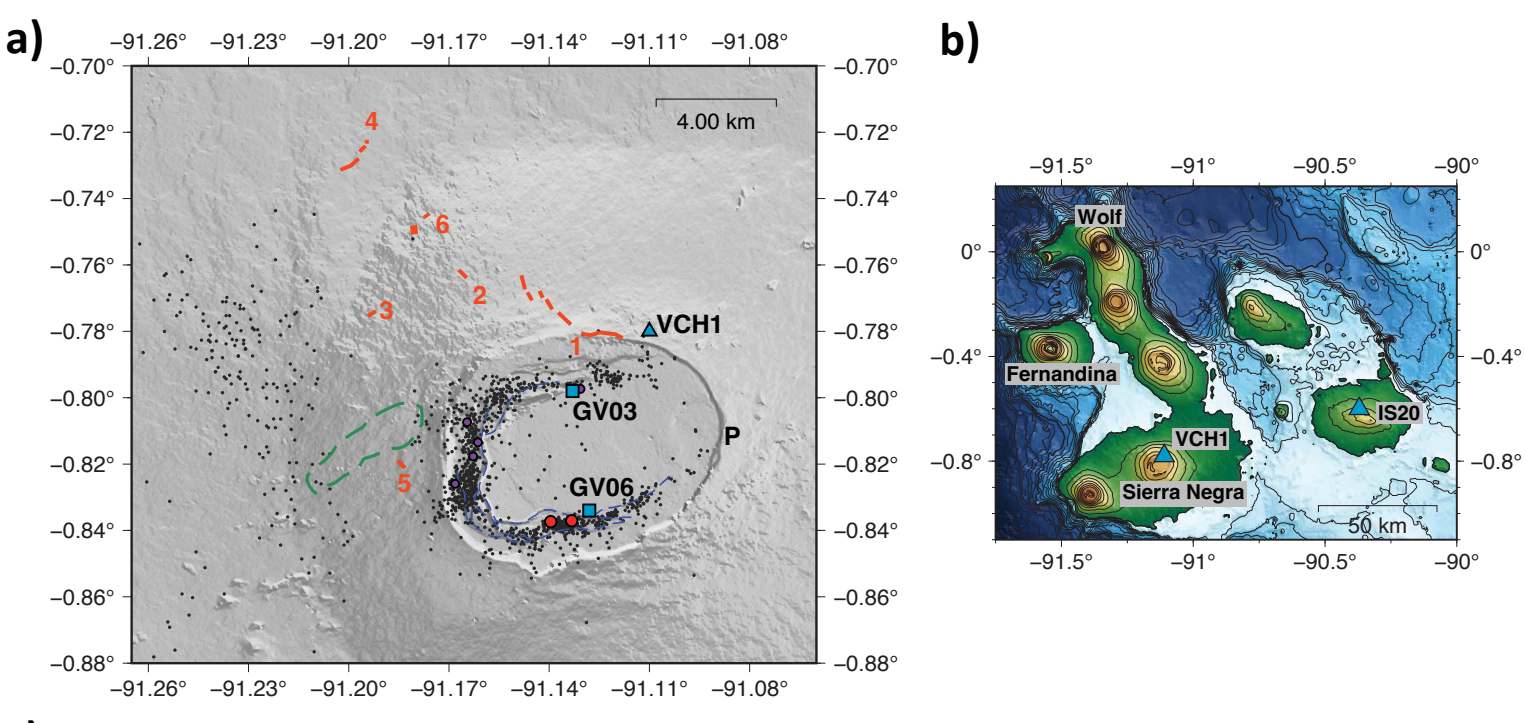




Figure 2	2.
----------	----

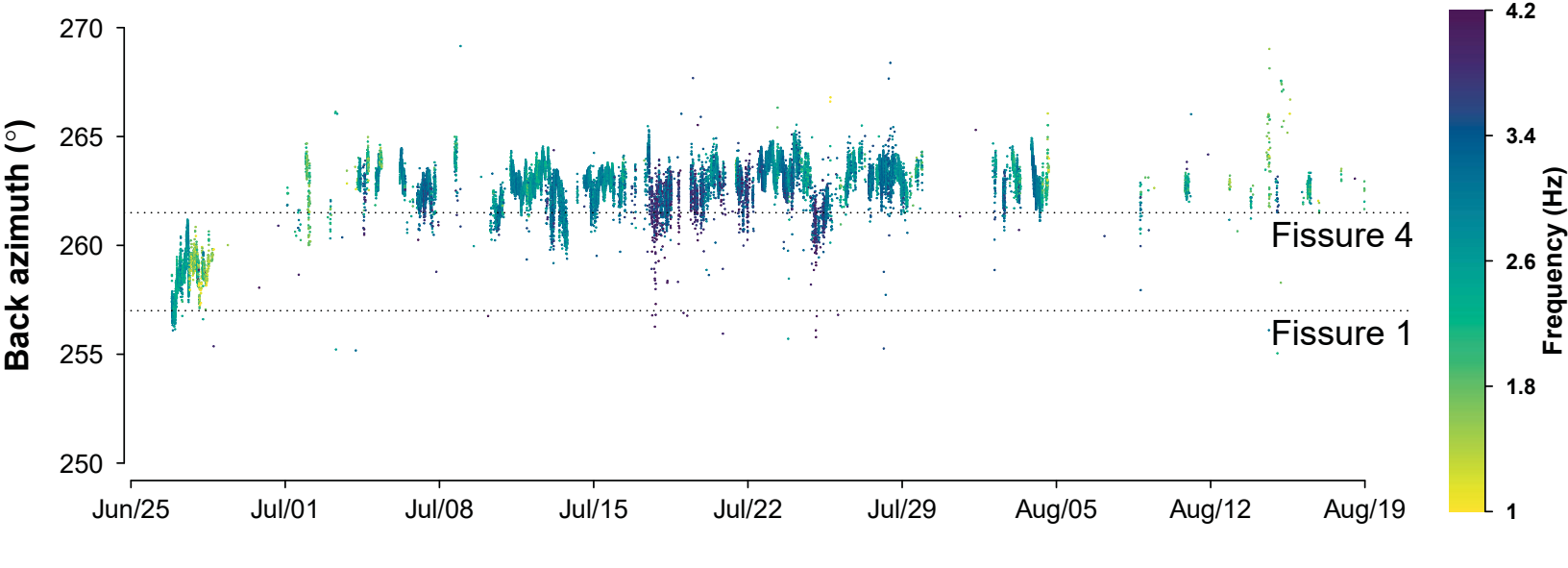


Figure 3	
----------	--

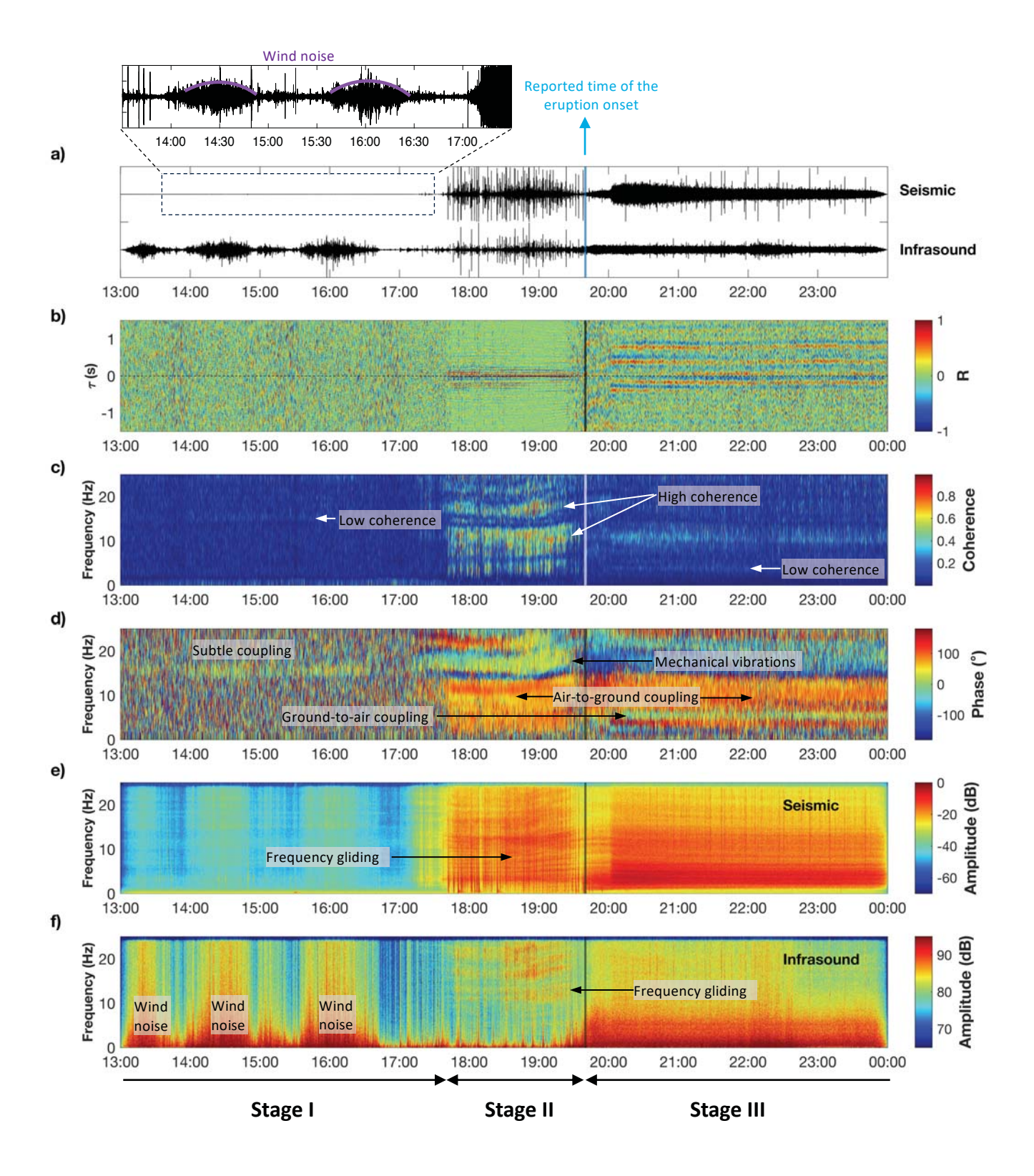


Figure 4.	
-----------	--

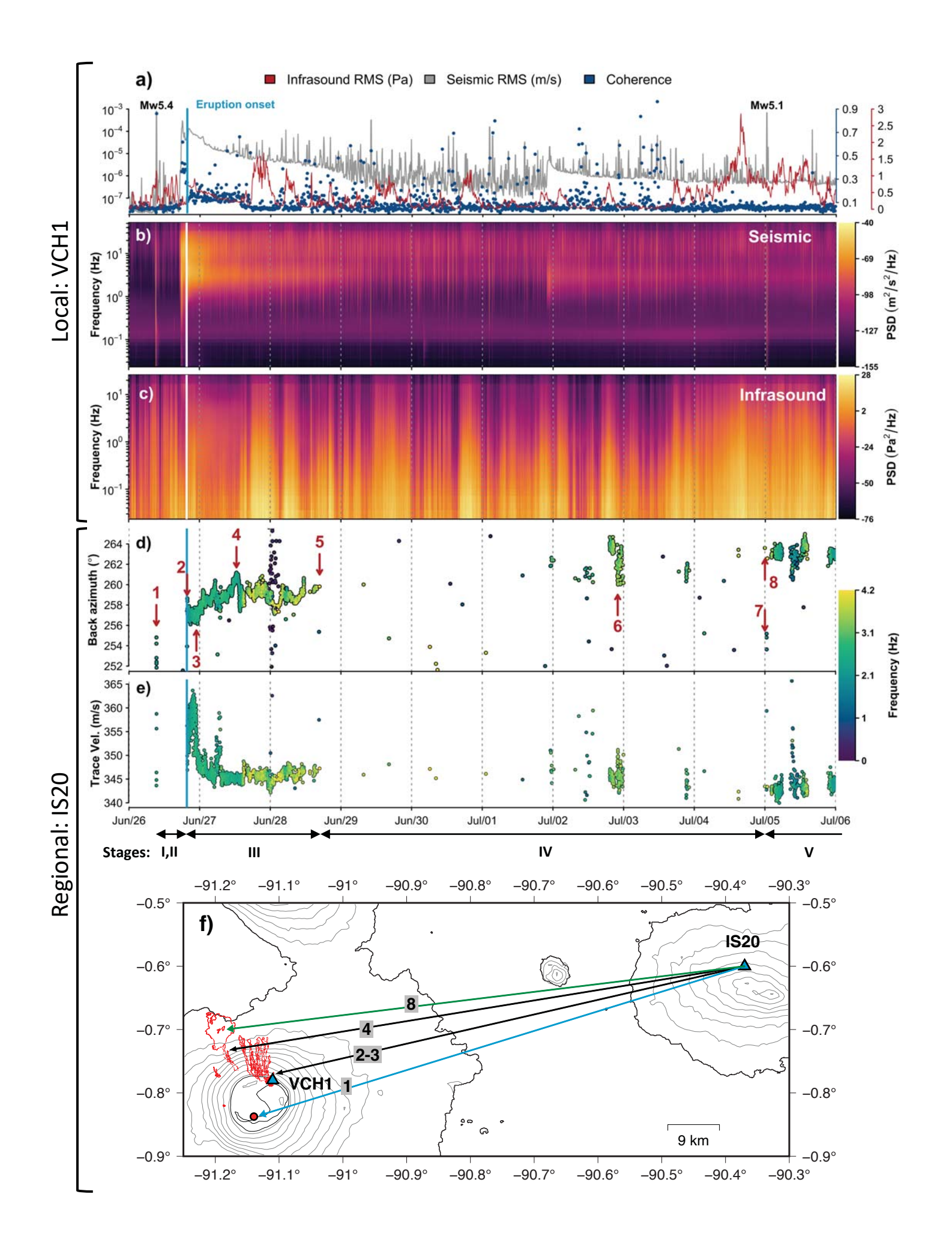


Figure 5.	
-----------	--

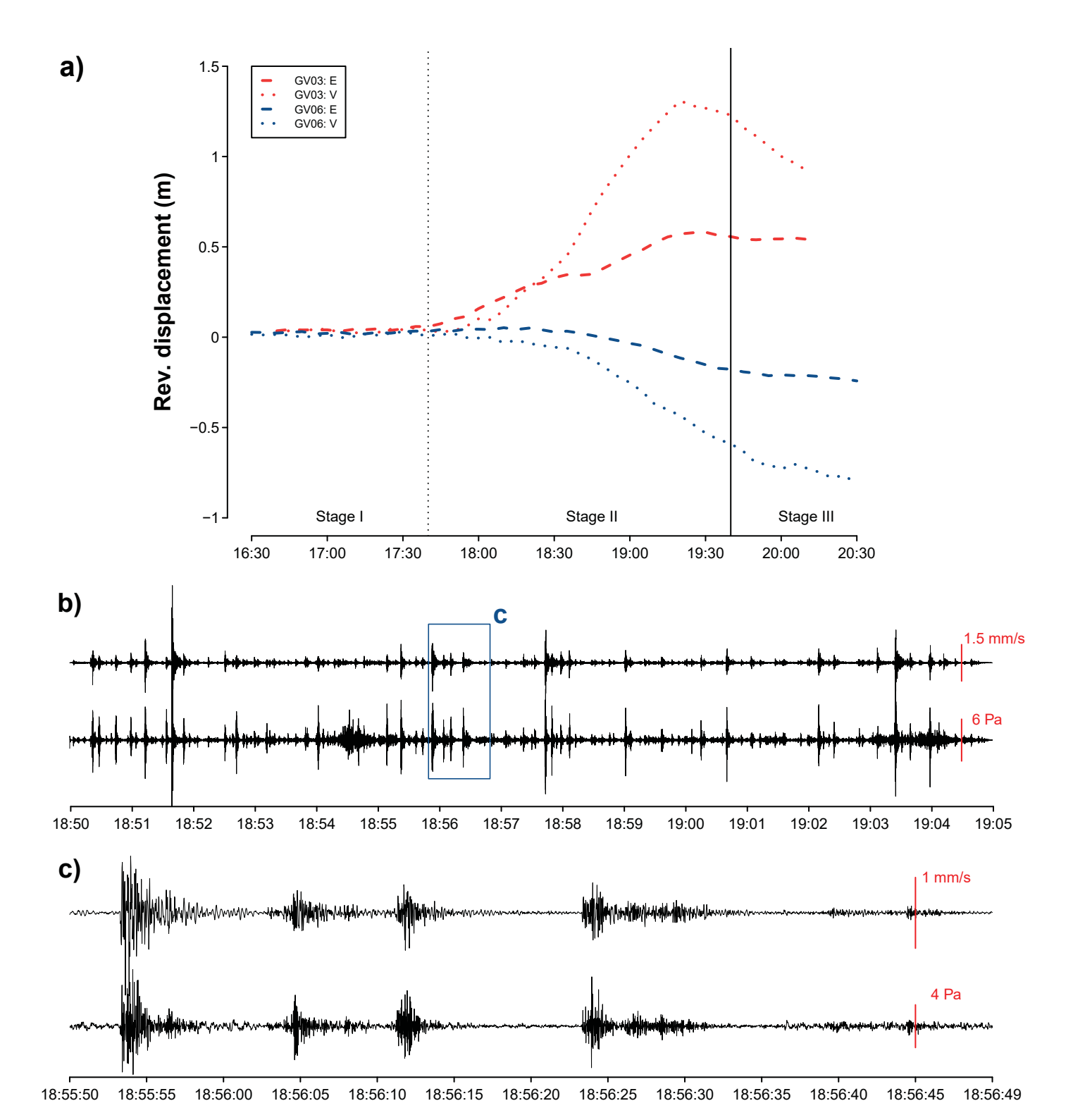


Figure 6.	
-----------	--

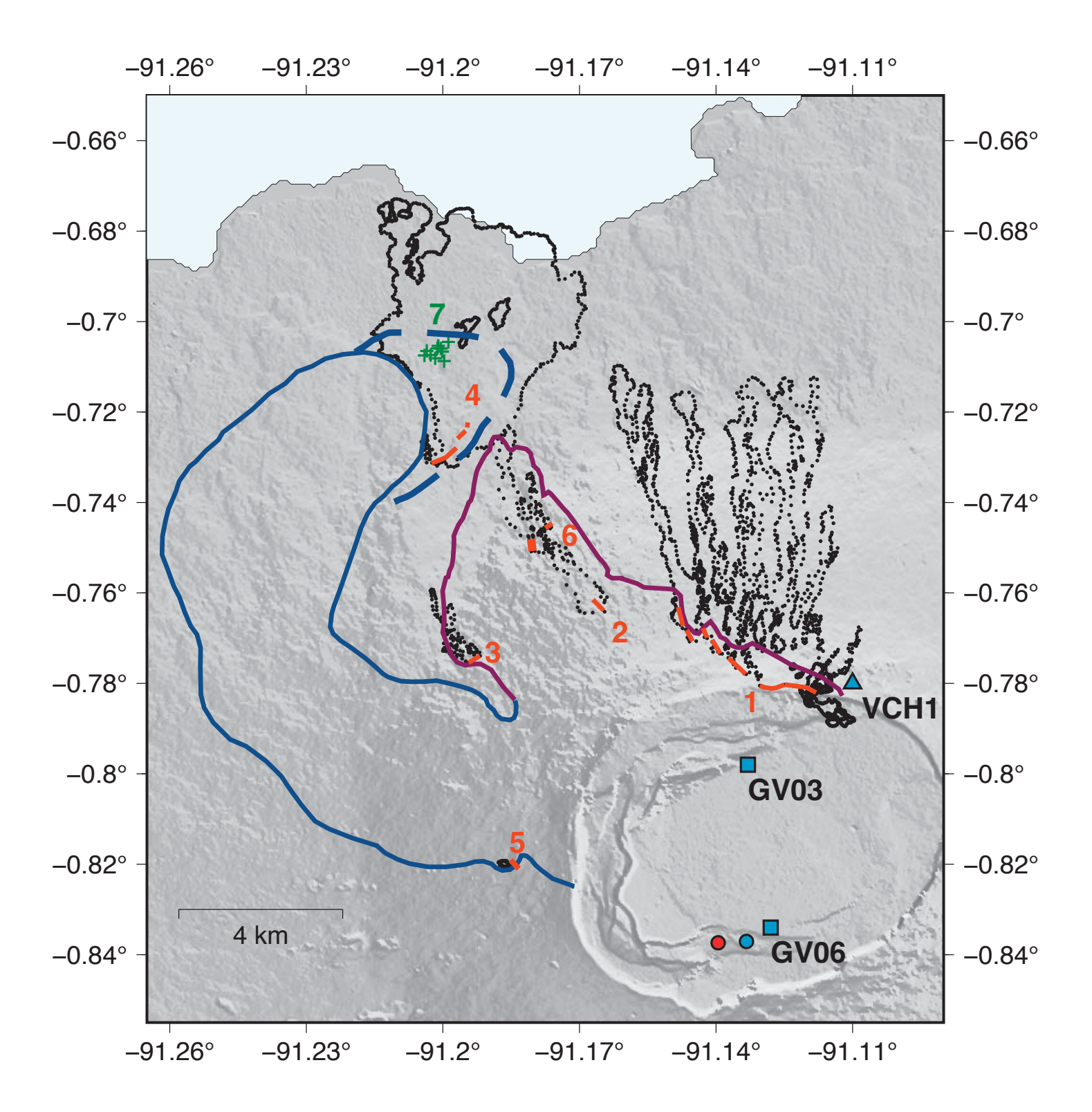


Figure 7.	
-----------	--

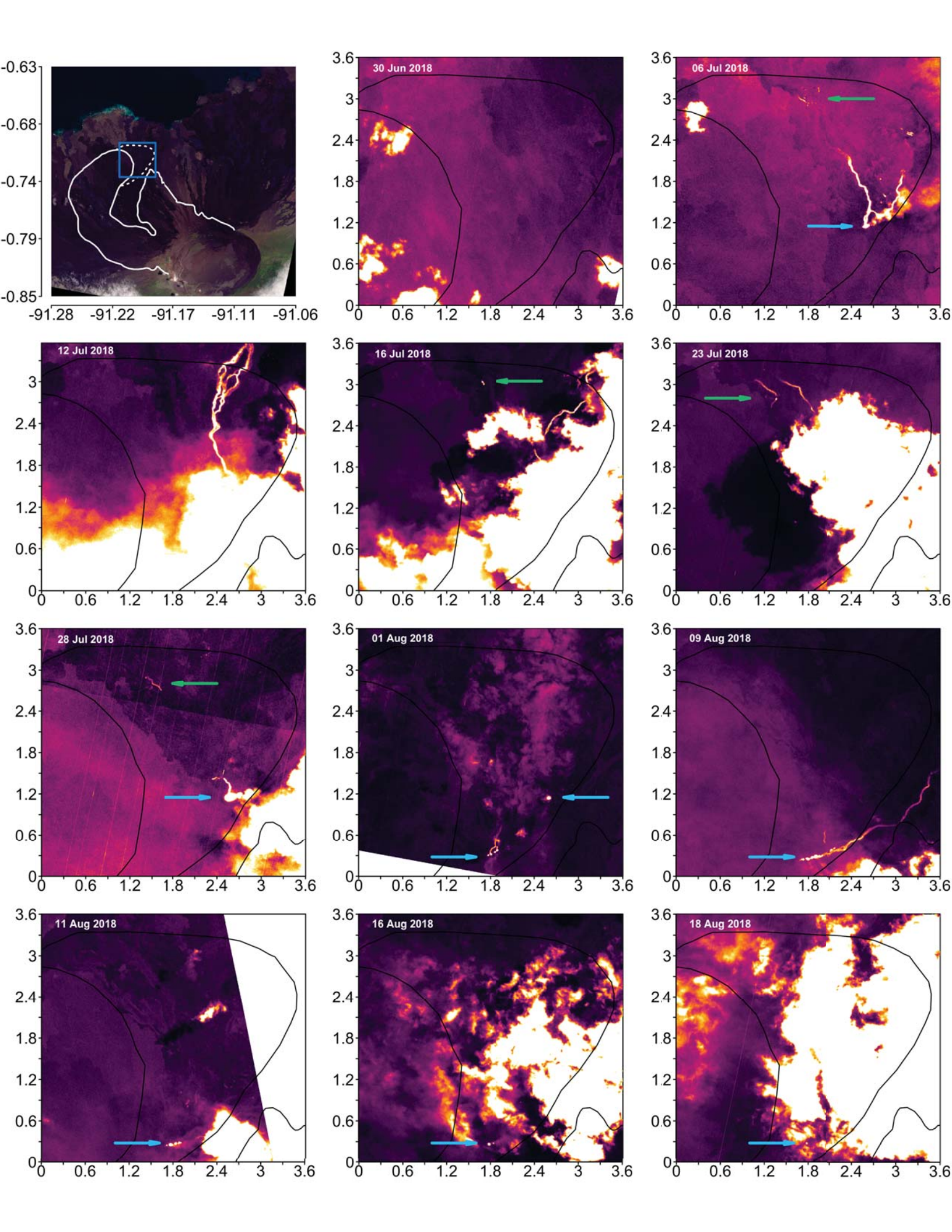


Figure 8	В.
----------	----

